


Route to chaos in the weakly stratified Kolmogorov flow

Cite as: Phys. Fluids **31**, 024106 (2019); <https://doi.org/10.1063/1.5081105>

Submitted: 14 November 2018 . Accepted: 24 January 2019 . Published Online: 15 February 2019

F. Gargano , G. Ponetti, M. Sammartino , and V. Sciacca 

COLLECTIONS

 This paper was selected as Featured



View Online



Export Citation



CrossMark

ARTICLES YOU MAY BE INTERESTED IN

[Simulation of high-speed droplet impact against a dry/wet rigid wall for understanding the mechanism of liquid jet cleaning](#)

Phys. Fluids **31**, 013303 (2019); <https://doi.org/10.1063/1.5079282>

[Referee acknowledgment for 2018](#)

Phys. Fluids **31**, 020201 (2019); <https://doi.org/10.1063/1.5090536>

[Local anisotropy of laboratory two-dimensional turbulence affects pair dispersion](#)

Phys. Fluids **31**, 025111 (2019); <https://doi.org/10.1063/1.5082851>

PHYSICS TODAY
WHITEPAPERS

ADVANCED LIGHT CURE ADHESIVES

Take a closer look at what these environmentally friendly adhesive systems can do

READ NOW

PRESENTED BY
 MASTERBOND
ADHESIVES | SEALANTS | COATINGS



Route to chaos in the weakly stratified Kolmogorov flow

Cite as: Phys. Fluids 31, 024106 (2019); doi: 10.1063/1.5081105

Submitted: 14 November 2018 • Accepted: 24 January 2019 •

Published Online: 15 February 2019



F. Gargano,^{1,a)}  G. Ponetti,^{2,b)} M. Sammartino,^{1,c)}  and V. Sciacca^{2,d)} 

AFFILIATIONS

¹Department of Engineering, University of Palermo, Palermo, Italy

²Department of Mathematics, University of Palermo, Palermo, Italy

^{a)}Electronic mail: francesco.gargano@unipa.it

^{b)}Electronic mail: giordanoponetti@gmail.com

^{c)}Electronic mail: marcomarialuigi.sammartino@unipa.it

^{d)}Electronic mail: vincenzo.sciacca@unipa.it

ABSTRACT

We consider a two-dimensional fluid exposed to Kolmogorov's forcing $\cos(ny)$ and heated from above. The stabilizing effects of temperature are taken into account using the Boussinesq approximation. The fluid with no temperature stratification has been widely studied and, although relying on strong simplifications, it is considered an important tool for the theoretical and experimental study of transition to turbulence. In this paper, we are interested in the set of transitions leading the temperature stratified fluid from the laminar solution $[U \propto (\cos(ny), 0), T \propto y]$ to more complex states until the onset of chaotic states. We will consider Reynolds numbers $0 < Re \leq 30$, while the Richardson numbers shall be kept in the regime of weak stratifications ($Ri \leq 5 \times 10^{-3}$). We shall first review the non-stratified Kolmogorov flow and find a new period-tripling bifurcation as the precursor of chaotic states. Introducing the stabilizing temperature gradient, we shall observe that higher Re are required to trigger instabilities. More importantly, we shall see new states and phenomena: the newly discovered period-tripling bifurcation is supercritical or subcritical according to Ri ; more period-tripling and doubling bifurcations may depart from this new state; strong enough stratifications trigger new regions of chaotic solutions and, on the drifting solution branch, non-chaotic bursting solutions.

Published under license by AIP Publishing. <https://doi.org/10.1063/1.5081105>

I. INTRODUCTION

We study the route to chaos of the Kolmogorov flow under the effect of density gradients. The Kolmogorov flow is a two-dimensional incompressible viscous flow on the torus $(x, y) = [0, 2\pi/\alpha] \times [0, 2\pi]$ driven by the streamwise monochromatic force $(n^3 \cos ny, 0)$, with α being the aspect ratio of the torus. It was introduced by Kolmogorov in 1959¹ as a toy-model capable of easing the mathematical difficulties of the full Navier-Stokes equations but still possessing the turbulent regimes typical of the Navier-Stokes solutions. The non-stratified Kolmogorov problem has been extensively studied in both laminar and turbulent regimes. In a pioneering paper,² flows on the domain $\mathbb{R} \times [0, 2\pi]$ were studied and the possible destabilization of the laminar solution $(U, 0) = (n \cos nz, 0)$

was shown. On the contrary, when the period number and the aspect ratio are both equal to 1 ($n = \alpha = 1$), the global stability of the laminar state holds for each forcing amplitude.³ When $\alpha < 1$, the stability of the secondary state has been studied by weakly non-linear methods.^{4,5} The non-linear dynamics for higher Reynolds (Re) numbers has been investigated via numerical simulation⁶⁻⁹ showing the emergence of complex time-dependent structures. The appearance of these states was also described by a finite dimensional dynamical system approach¹⁰⁻¹³ and by multiple-scale analysis.⁴ It is clear that the quantities n and α are crucial parameters of the system as they determine the structure of the base solution and the wavelengths admissible for the domain. In this paper, as we shall see later, we shall make the simplest possible choice, i.e., $n = 2$ and $\alpha = 1$.

One of the features of the classical Kolmogorov model is the ability to coalesce small scale structures to the largest scale available to the physical system. For this reason, the model has been used to understand coalescence effects observed in many fields of fluid dynamics. For example, Kolmogorov's model has been applied in geophysical fluid dynamics to study the stability of finite-amplitude Rossby waves in the atmosphere¹⁴ or three-jet zonal flows on a rotating sphere¹⁵ or to see whether baroclinic instabilities might cascade into easterly flows of planetary-scale.¹⁶ The model was also reproduced in laboratory showing the effect of drag forces on the linear stability of the laminar solution.¹⁷ This external effect may be removed using immiscible multilayer fluids¹⁸ or soap films.¹⁹ We also mention the fact that, to mimic and study the stability of zonal jets along the tropopause, the Kolmogorov flow, in a laboratory experiment, has been induced on a spherical surface.²⁰

The stratified counterpart of the Kolmogorov flow, which is the subject of our analysis, has been reproduced in laboratory experiments in the limit of weak²¹ as well as strong²² stratifications. In the former case, experiments show the critical Reynolds number for the linear instability of the laminar flow to increase with the Richardson (Ri) number; in the limit of $Ri \ll 1$, and accounting for the wall friction effects, the prediction of theory matches with experimental observations. In the latter case of strong stratification, the wall friction is irrelevant for the linear stability of the laminar solution. This has been observed also by solving the eigenvalue problem of the stratified Kolmogorov model affected by a linear drag.^{23,24}

Concerning the non-stratified Kolmogorov flow, different parameter setups have been considered: the domain aspect ratio,²⁵ the inclination of the force,¹⁰ and its periodicity.²⁶ In the space of π -rotation invariant solutions, the effect of the aspect ratio ($\alpha < 1$) on the bifurcation cascade has been studied.²⁷ Without this symmetry restriction, in the low Reynolds number range ($Re < 30$), and fixing $\alpha = 1$ and $n = 2$, the bifurcation diagram has been constructed via symmetry group analysis, while chaotic states have been analyzed via Karhunen-Loève expansions.⁶ The stability of a three-jet zonal flow ($n = 3/2$) imposed on a rotating sphere is investigated for various Reynolds numbers and rotation rates showing a complex bifurcation structure, whereas non-rotational induced chaos at high Re is effectively mimicked by a low-dimensional space of steady and steady-traveling solutions.¹⁵ For fluids affected by external forcing inclined with respect to the axes and period $n > 1$, the appearance of time dependent solutions was also described in terms of finite dimensional dynamical systems.¹⁰ For fully developed turbulence, recurrent unstable solutions are extracted from the fluid motion in order to mimic the possible turbulent trajectories of the flow.²⁸

On the other hand, in the density stratified Kolmogorov flow, the bifurcations leading to chaotic states have not been studied. In this paper, we shall be interested in the bifurcations that occur at low Reynolds numbers ($Re/Re_c < 21$), when the Kolmogorov flow is induced in a fluid where the stratification has a stabilizing effect: the density decreases with height. Therefore the main topic of this paper is the set of

bifurcations leading from laminar solutions toward weakly chaotic states.

We shall describe the base density profile as a linear function decreasing from the bottom to the top of the fluid. More specifically, we shall fix our model to the configuration⁶ $\alpha = 1$ and $n = 2$. This model has geophysical application related to the stability of internal gravity waves with finite amplitude¹¹ and vertical shear flows,²⁹ whilst in the limit of low Péclet numbers it is relevant for astrophysical systems.³⁰ We recall the fact that the primary bifurcation, in the limit of very weak density gradients, has been investigated using linear stability analysis.³¹ Weakly non-linear theory leads to the Cahn-Hilliard equation and shows the effect of the stratification as a regulator of the inverse energy cascade.

The first part of the paper is devoted to a review of the bifurcation diagram of the non-stratified flow. In the second part of the paper, we shall consider the influence of temperature stratification on the bifurcation diagram, in the range of small Richardson numbers. By linear stability analysis, the laminar state is globally stable if the Richardson number is above a threshold, which for our system is $Ri = 4$. In the region $Ri < 4$, the influence of temperature gradients on the transitions leading to chaotic attractors has not been extensively investigated yet. In the range of Richardson number values $0 \leq Ri < 4$, we have analyzed the dynamics of the system in the case of weak stratification, with the main interest of the paper being the onset of new features triggered by the stratification. In particular, we have focused in the range $0 < Ri \leq 5 \times 10^{-3}$. When the stratification values are $Ri \leq 10^{-4}$, our analysis has revealed no significant change with respect to the case $Ri = 0$; see also Ref. 32. On the contrary, when $10^{-3} \leq Ri \leq 5 \times 10^{-3}$, we shall observe new transitions and new interesting phenomena. Moreover a preliminary investigation at $Ri = 10^{-2}$ or higher has revealed the emergence of completely new dynamic behaviors with characteristics that make it difficult for comparison with the non-stratified Kolmogorov flow. We therefore believe that the physics at $Ri > 0.005$ deserves a separate analysis to be left to future investigations.

For the non-stratified flow, we will show the presence of a period-tripling bifurcation that went unnoticed in previous studies and use the Lyapunov exponent analysis to prove the chaotic nature of a further bifurcation departing from the period-tripled state. This bifurcation is a rare transition toward chaotic states in fluid dynamical systems, even though it can be found in other fields. It is a common feature in directly modulated diode lasers,^{33,34} and the process of period n -tupling is a feature of the Toda oscillator.³⁵ In the field of fluid dynamics, it has been observed (together with period-doubling and quintupling) in the Rayleigh-Bénard convection³⁶ and in sinusoidally varying volumetric flow induced in curved tubes.³⁷ Moreover non-linear mode interactions produce period-tripling flutters in transonic flows.³⁸ It is not clear whether a route to chaos could be driven by a period-tripling cascade as in the period-doubling Feigenbaum scenario. However period tripling has been observed as a "window" in the Feigenbaum route to chaos where, for a range of the control parameters, the system reaches a periodic motion from a more chaotic state.³³

For the stratified Kolmogorov flow, we shall compare the bifurcations to the non-stratified scenario and analyze the new transitions allowed by introducing the temperature gradient. Besides the obvious observation that higher Reynolds numbers are required to trigger the instabilities, we shall see that, by increasing the temperature gradient, a richer variety of states leads eventually to the chaotic attractors.

The outline of the paper is as follows: In Sec. II, we state the problem under investigation. The 2D incompressible Navier-Stokes equations and the energy conservation equation are presented; the Boussinesq approximation is introduced leading to the PDE system (8) and (9); and finally the numerical algorithm we use to solve it is briefly described. In Sec. III, we give a detailed review of the non-stratified Kolmogorov flow, elucidating the states corresponding to each bifurcation in the low Reynolds number range $Re \leq 30$ and presenting a newly observed period-tripling bifurcation. In Sec. IV, we present our numerical results and show that besides an overall stabilizing effect, some states are stable in smaller regions of the parameters and instabilities can lead to new states as non-chaotic bursting and cascades of period-doublings and triplings. Finally, in Sec. V, we draw some conclusions and suggest possible future directions of research, also in other flow regimes.

II. FORMULATION

We consider the incompressible Navier-Stokes flow on the plane (x, y) with a gravity field $-g$ along the cross-stream direction y . To account for temperature variations, we use conservation of energy. The resulting system, written under the Boussinesq approximation, is

$$\frac{\partial \mathbf{u}^*}{\partial t^*} + \mathbf{u}^* \cdot \nabla^* \mathbf{u}^* + \frac{1}{\rho_r} \nabla^* p^* = \nu \Delta^* \mathbf{u}^* - g \frac{\rho - \rho_0}{\rho_r} \hat{\mathbf{y}} + \gamma n^3 \cos(2\pi n y^*/L_y) \hat{\mathbf{x}}, \quad (1)$$

$$\nabla^* \cdot \mathbf{u}^* = 0, \quad (2)$$

$$\frac{\partial T^*}{\partial t^*} + \mathbf{u}^* \cdot \nabla^* T^* = \kappa_T \Delta^* T^*, \quad (3)$$

where the star is for physical quantities. The velocity field is $\mathbf{u}^* = (u^*, v^*)$, p^* is the pressure scalar field, and ρ is the density of the fluid. The parameters γ and n represent the magnitude and the wavenumber of the external force, respectively. The material parameters are ν , the kinematic viscosity, and κ_T , the thermal conductivity. The scalar and vector fields are defined on the doubly periodic domain $(x^*, y^*) \in \mathcal{D}^* = [0, L_x] \times [0, L_y]$, while $\alpha = L_y/L_x$ defines the aspect ratio.

We consider the effects of a stabilizing temperature gradient: the fluid is cold (T_b) at the bottom and warm at the top (T_t); thus, $\Delta_T = T_t - T_b > 0$. We assume that the basic temperature profile over the length L_y is given by the linear interpolation $T_0^*(y^*) = T_b + \Delta_T y^*/L_y$; perturbations from the basic profile are denoted by $\theta(x^*, y^*, t^*)$ so that the perturbed temperature profile is $T^*(x^*, y^*, t^*) = T_0^*(y^*) + \Delta_T \theta(x^*, y^*, t)/2\pi$. The Boussinesq approximation, adopted in this paper, relies on two assumptions: first, the linear relationship between density and temperature:

$\rho(T^*) = \rho_r[1 - \beta(T^* - T_r)]$, where T_r and ρ_r are the reference temperature and the density, β is the thermal expansion coefficient, and the basic density profile is given by $\rho_0(y^*) = \rho(T_0^*)$; second, on neglecting density variations induced by temperature, except in the buoyancy term.

The equations are nondimensionalized using $\mathcal{L} = \frac{L_y}{2\pi}$ as the lengthscale, $\mathcal{T} = \frac{1}{\nu} \left(\frac{L_y}{2\pi}\right)^2$ as the time scale, $\mathcal{U} = \frac{\gamma}{\nu} \left(\frac{L_y}{2\pi}\right)^2$ as the reference velocity, and $\mathcal{P} = \rho_r \gamma \frac{L_y}{2\pi}$ as a reference pressure. The above equations can therefore be rewritten in non-dimensional form as

$$\frac{\partial \mathbf{u}}{\partial t} + Re \mathbf{u} \cdot \nabla \mathbf{u} + \nabla p = \Delta \mathbf{u} + Ri Re \theta \hat{\mathbf{y}} + n^3 \cos(ny) \hat{\mathbf{x}}, \quad (4)$$

$$\nabla \cdot \mathbf{u} = 0, \quad (5)$$

$$\frac{\partial \theta}{\partial t} + Re \mathbf{u} \cdot \nabla \theta = \frac{\Delta \theta}{Pr} - Re v, \quad (6)$$

defined on the doubly periodic domain $\mathcal{D} := [0, 2\pi] \times [0, 2\pi L_y/L_x]$, where the nondimensional parameters

$$Re = \frac{\mathcal{U} \mathcal{L}}{\nu} = \frac{\gamma}{\nu^2} \left(\frac{L_y}{2\pi}\right)^3, \quad (7)$$

$$Ri = \frac{g\beta\Delta_T\mathcal{L}}{2\pi\lambda^2} = \frac{g\beta\Delta_T}{2\pi} \left(\frac{\nu}{\gamma}\right)^2 \left(\frac{2\pi}{L_y}\right)^3, \quad Pr = \frac{\nu}{\kappa_T}$$

are, respectively, the Reynolds number, the Richardson number, and the Prandtl number. Since the fluid is two-dimensional and solenoidal, we can adopt the vorticity-stream function formulation. Recalling that the vorticity is defined as $\omega = \nabla \times \mathbf{u}$ and that the stream function Ψ is related to the velocity by $\mathbf{u} = (u, v) = (\Psi_y, -\Psi_x)$, one can find Ψ in terms of the vorticity by solving the Poisson problem $\omega = -\Delta\Psi$. Taking the curl of (4), we get

$$\frac{\partial \Delta \psi}{\partial t} - Re J(\Psi, \Delta \Psi) = \Delta^2 \psi - Ri Re \theta_x, \quad (8)$$

$$\frac{\partial \theta}{\partial t} - Re J(\Psi, \theta) = \frac{\Delta \theta}{Pr} + Re \psi_x, \quad (9)$$

where $J(a, b) = a_x b_y - a_y b_x$. To write the above system, we have used the decomposition $\Psi(x, y, t) = \sin ny + \psi(x, y, t)$, with $\psi(x, y, t)$ being the deviation of the stream function from the laminar state. Here we follow⁶ and fix the period of the external force $n = 2$ and choose the aspect ratio $\alpha = 1$. We set throughout the paper the Pr number to be 1 so that momentum and thermal diffusivity have the same amplitude (some discussion for larger Pr is given in the conclusion).

We solve numerically Eqs. (8) and (9) with a classical fully de-aliased Fourier-Fourier pseudospectral code³⁹ with a second-order semi-implicit time integrator. Time-integration is based on a second-order Runge-Kutta algorithm where the discretization of the linear part is of the Crank-Nicolson type. De-aliasing is performed with the usual 2/3 rule. The spatial resolution adopted here is $N_x = N_y = 64$, whilst the time step is $\Delta t = 0.001$. We have always tested grid-independence of our results using higher resolutions $N_x = N_y = 128$ or even $N_x = N_y = 256$. The resolution $N_x = N_y = 256$ (with

grid-independence tested using $N_x = N_y = 512$) turned out to be necessary for some simulations of the high Re or Pr regimes, reported and briefly discussed in the Conclusion.

The bifurcation parameter is the Reynolds number, whilst the Richardson number is kept fixed to some particular values ($Ri = 0, 10^{-4}, 10^{-3}, 5 \times 10^{-3}$). For relatively high Re (typical Re larger than 21), chaotic solutions will arise and we shall detect transitions to chaos by computing the Lyapunov exponents.

We shall construct the bifurcation diagram using the L^2 -norm of $X = (\psi, \theta)^T$ defined as

$$\|X\|_2^2 = \|\psi\|_2^2 + \|\theta\|_2^2, \tag{10}$$

where

$$\|\psi\|_2^2 = \sum_{j=-N_x/2+1}^{N_x/2} \sum_{l=-N_y/2+1}^{N_y/2} |\widehat{\psi}_{j,l}|^2, \quad \|\theta\|_2^2 = \sum_{j=-N_x/2+1}^{N_x/2} \sum_{l=-N_y/2+1}^{N_y/2} |\widehat{\theta}_{j,l}|^2, \tag{11}$$

where $\widehat{\psi}_{j,l}$ and $\widehat{\theta}_{j,l}$ are the Fourier coefficients of ψ and θ , respectively.

Since the study of the sign of Lyapunov exponents is an effective diagnostic tool for chaotic systems, we compute them across supposed bifurcations to chaotic states. The idea is to consider a trajectory of the solution of a dynamical system, perturb it of an infinitesimal amount, and measure in time how this perturbation evolves. It is in the definition of chaotic states that infinitely near trajectories diverge eventually; therefore, we measure the growth or decay of these small perturbations. Given an initial value X_0 in the phase space, its evolution is given by $X_{n+1} = f(X_n)$. If the vector $\delta X_n^{(j)}$ is a small perturbation from X_n in the j th direction, we find that

$$\delta X_n^{(j)} = Df_{X_{n-1}} \delta X_{n-1}^{(j)} = Df_{X_0}^n \delta X_0^{(j)}. \tag{12}$$

This is the vector that we keep measure of and defines the Lyapunov exponent spectrum $\{\lambda_1, \lambda_2, \dots, \lambda_m\}$, where $\lambda_1 \geq \lambda_2 \geq \dots \geq \lambda_m$ and

$$\pm \lambda_j = \lim_{n \rightarrow \pm\infty} \frac{1}{|n|} \log \|Df_{X_0}^n \delta X_0^{(j)}\|_2. \tag{13}$$

The associated perturbation vector in X_n , $\delta X_n^{(j)}$, is the Lyapunov vector which point toward the direction j where the perturbation grows at a λ_j rate. The algorithm to extract these values⁴⁰ takes a post-transient initial condition X_0 and a ball of initial perturbations $\delta X_0^{(j)}$ and evolves the former by using the pseudospectral code we presented in the previous paragraph and the latter using their linearized instance.

To get a better understanding of the phenomenology we shall observe, we find it useful to monitor the time evolution of the kinetic energy E_K , the potential energy E_P , the enstrophy \mathcal{E} , the palinstrophy \mathcal{P} , the kinetic energy injection rate \mathcal{F} , the potential energy dissipation rate \mathcal{E}_θ , and the energy exchange rate \mathcal{X} defined as

$$E_K = \frac{1}{2} \|\mathbf{u}\|_2^2, \quad E_P = \frac{1}{2} Ri \|\theta\|_2^2, \quad \mathcal{E} = \|\omega\|_2^2, \quad \mathcal{P} = \|\nabla\omega\|_2^2, \\ \mathcal{E}_\theta = \frac{Ri}{Pr} \|\nabla\theta\|_2^2, \quad \mathcal{F} = n^3 \langle \cos(ny), u \rangle, \quad \mathcal{X} = -Ri Re \langle \theta, v \rangle,$$

where $\langle f, g \rangle := \frac{1}{|\mathcal{D}|} \int_{\mathcal{D}} f g dx dy$ and $\|\cdot\|_2^2 = \langle \cdot, \cdot \rangle$. One can write the following equations for the evolution of the kinetic energy, of the potential energy, and of the enstrophy:

$$\frac{dE_K(t)}{dt} = -\mathcal{E}(t) + \mathcal{F}(t) - \mathcal{X}(t), \tag{14}$$

$$\frac{dE_P(t)}{dt} = -\mathcal{E}_\theta(t) + \mathcal{X}(t), \tag{15}$$

$$\frac{d\mathcal{E}(t)}{dt} = -2\mathcal{P}(t) + 2n^4 \langle \omega, \sin(ny) \rangle + 2Ri Re \langle \omega, \theta_x \rangle. \tag{16}$$

The inflow of energy \mathcal{F} , due to the external forcing, increases kinetic energy which, besides being dissipated by vortical structures, can now be transferred to potential energy; in fact, for all the configurations we shall encounter (the only exception is reported in the Conclusions), we shall see that the energy exchange rate \mathcal{X} is always positive, meaning that the energy always flows from kinetic to potential. Potential energy is dissipated by temperature gradients.

Enstrophy and palinstrophy growth phases are main indicators of the formation and of the rearrangement of vortical structures in the flow. Generation of vorticity is accompanied by the growth in the enstrophy distribution,⁴¹⁻⁴⁶ while the rearrangement of the existing structures can lead to phases of increasing palinstrophy (the so-called *mixing events*^{47,48}). In all our simulations, including the stratified case, peaks of \mathcal{P} are always indicators of the strengthening of the dipolar structures in the flow: this will be discussed and shown in several cases along the paper. The efficiency of the exchange between kinetic and potential energy [i.e., the exchange factor \mathcal{X} in (14) and (15)] depends on the strength of stratification Ri combined with the Reynolds number Re . Similarly (16) shows how stratification (again combined with Re) can drive enstrophy production (or enstrophy destruction, depending on the alignment between the vorticity and the horizontal temperature gradient). This gives a qualitative explanation why a weak stratification and moderate-low Re numbers can hardly influence the flow evolution as compared with the non-stratified case: this is the case we shall observe for $Ri = 10^{-4}$ and $Re < 30$. On the other hand, even a moderately higher stratification, e.g., $Ri \geq 10^{-3}$, can lead to significant enstrophy and palinstrophy growth and therefore to formation of new structures and to their rearrangement. It is also interesting to notice how, in all our numerical experiments, the time evolution of enstrophy is positively correlated to the time evolution of palinstrophy: the strengthening (or the weakening) of the vortical structures inevitably leads to stronger vorticity gradients and therefore to larger (or smaller) palinstrophy. On the contrary, the time evolution of potential energy is negatively correlated to the time evolution of enstrophy; this means that enstrophy (and palinstrophy) growth phases are accompanied by the occurrence of strong temperature gradients (the only possible mechanism of potential energy dissipation). The system, after the occurrence of a phase of energy accumulation, tends to use both energy dissipation mechanisms, i.e., the enstrophy \mathcal{E} and the thermal dissipation \mathcal{E}_θ .

The range of the parameters considered in this paper typically includes some laboratory flows. For example, $Pr \approx 1$ is characteristic of gases at room temperature, while the range of Re and Ri considered here represents flows contained in tanks of few centimeters in size and with temperature gradient of few degrees; for example, one could consider air (with $Pr \approx 0.7$, $\nu \approx 1.5 \times 10^{-1} \text{ cm}^2/\text{s}$, and $\beta \approx 3 \times 10^{-3} \text{ }^\circ\text{C}^{-1}$), in a tank of size $L_x = L_y \approx 2.7 \text{ cm}$, subject to the forcing $\gamma \approx 10 \text{ cm/s}^2$ and to a temperature gradient $\Delta_T \approx 1.0 \text{ }^\circ\text{C}$: this setting would result in $Ri \approx 5 \times 10^{-3}$ and $Re \approx 40$.

Passing to flows at the geophysical scale, in the lower atmosphere $L_y \approx 100 \text{ m}$, there have been cases reported⁴⁹ of thermal inversion where the competing effects of the wind-shear and of the temperature gradient result in Ri ranging from 0 up to 2; in these cases, Re however is obviously very high and outside the range considered in this paper.

III. KOLMOGOROV FLOW

The non-stratified Kolmogorov flow is an important model that has been used to investigate transition and turbulent phenomena in the Navier-Stokes equations. In this section, we summarize the sequence of bifurcations of the non-stratified Kolmogorov flow⁶ that leads the laminar solution to chaotic states.

Here we also mention that we have found one of the oscillatory states to undergo a period-tripling bifurcation. This is

a transition which went unnoticed in previous studies and which will be analyzed in more detail in this section. The solutions of the Kolmogorov flow for $Re \leq 30$ are schematically reported in panel (a) of Fig. 1 [panels (b) and (c) are magnifications of panel (a)], where we show their bifurcation diagram. We control the solutions by the Reynolds number and track them by $\|\psi\|_2$. When ψ is time dependent, we report a suitable time average of $\|\psi\|_2$.

We recall² that on a horizontally unbounded domain ($\alpha = 0$), the Kolmogorov flow loses its stability at $Re_c^{unb} = \sqrt{2}$. For the case analyzed in this paper, $\alpha = 1$ and $n = 2$, through the Galerkin projection, a 5-dimensional dynamical system was derived,⁶ whose linear stability analysis shows that the critical value of the bifurcation parameter rises to $Re_c = 5/\sqrt{6}$.

The bifurcation diagram, reported in Fig. 1, shows two main branches: the first one originates from a drifting bifurcation, and we shall denote the states on this branch as D_i ; the second one connects with the main steady solution (we shall denote the states on this branch as S_i), and it is unstable till the state S_1 where it regains its stability. More specifically in Fig. 1, one can recognize the following main states:

1. For $Re < Re_c = 5/\sqrt{6}$, a sinusoidal shear velocity profile, commonly referred to as the *Kolmogorov flow*, with the same shape of the external force. We name this point

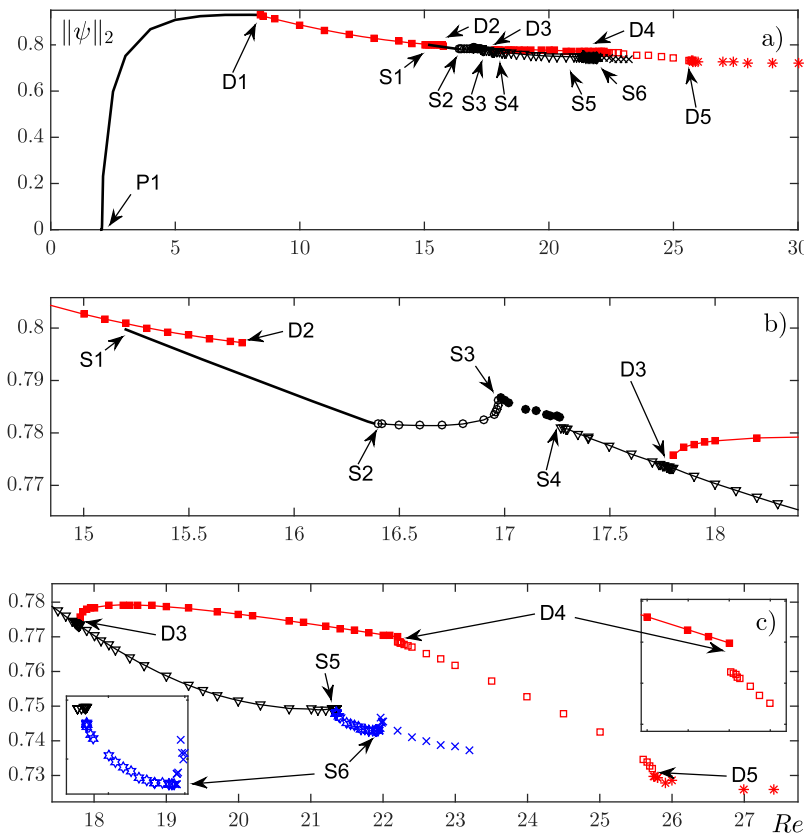


FIG. 1. (a) The full bifurcation diagram for the non-stratified Kolmogorov flow. On the horizontal axis is the Reynolds number, while on the vertical axis we report the L^2 -norm of the stream function. Panels (b) and (c) are magnifications of relevant parts of the bifurcation diagram. In panel (a), the solid bold line denotes the steady state solution departing from the primary bifurcation of the laminar state, while in panel (b) it denotes the solution appearing through hysteresis from the drifting state in S_1 . Red filled squares stand for the first and second drifting states, and red empty squares stand for oscillatory drifting states which become chaotic through intermittency (red asterisks). Black empty circles stand for the Hopf bifurcation of the steady state, and black filled circles stand for the gluing process of the Hopf solutions. Black inverted triangles stand for stable glued states. Blue stars stand for the period-tripled state, and blue crosses stand for its chaotic bifurcation.

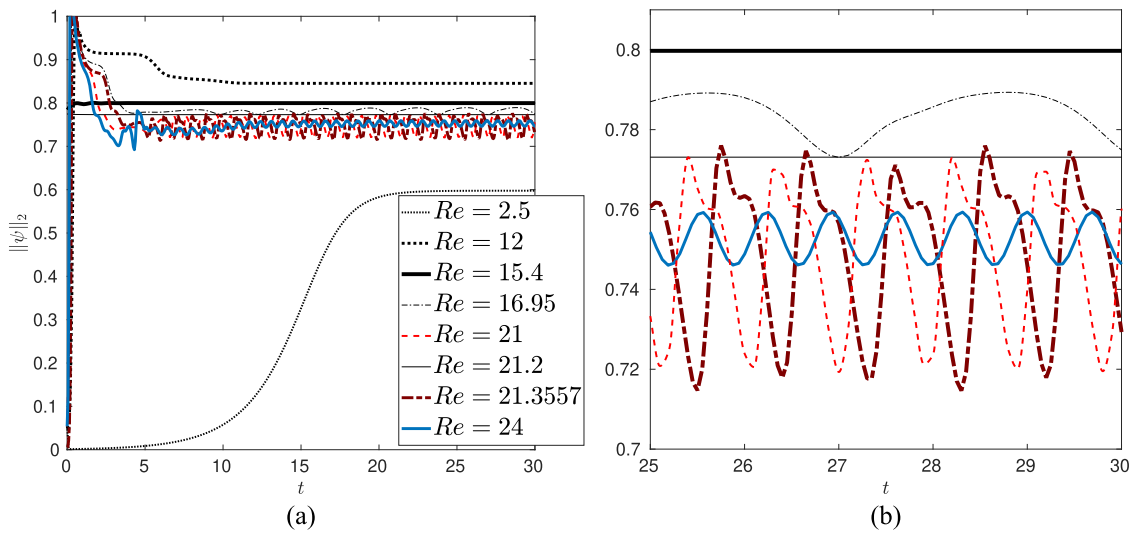


FIG. 2. In panel (a), we report the time evolution of $\|\psi\|_2$ toward the stationary or periodic state; (b) the magnification of (a) in the time interval $25 \leq t \leq 30$. The different curves are associated with the first steady state at $Re = 2.5$, first drifting state at $Re = 12$, second steady state at $Re = 15.4$, periodic orbit at $Re = 16.95$, glued periodic orbit at $Re = 21$, second drifting state at $Re = 21.2$, period-tripled state at $Re = 21.3557$, and oscillating drifting state at $Re = 24$.

- P1 and indicate its corresponding parameter value by $Re(P1, Ri = 0) = 5/\sqrt{6}$.
- For $Re > Re_c$, the laminar state bifurcates toward a stationary pattern (denoted, in Fig. 1, with a solid bold line) consisting in vortex cores of alternating sign forming vertical dipolar structures. In panel (a) of Fig. 2, we show, for different Re , typical time evolutions of the L^2 -norm $\|\psi\|_2$ of a random perturbation of the laminar state. The curve at $Re = 2.5$ represents the stabilization toward the above described stationary pattern.
 - When the Reynolds number increases, in D1, at a parameter value of $Re(D1, 0) = 8.3$, the solution bifurcates to a stable drifting state [denoted, in Fig. 1, with (red filled squares)]. This state is characterized by a uniform (in time and space) horizontal motion of the vorticity configuration. In panel (a) of Fig. 2, we report, at $Re = 12$, the typical time evolution of $\|\psi\|_2$.
 - The drifting state loses its stability at $Re(D2, 0) = 15.8$, and the system shows a hysteretic transition toward a branch of steady solutions. Following this branch backward, one finds that it forms at $Re(S1, 0) = 15.2$. Moreover the symmetries of the governing equations⁶ allow four different steady solutions (all of them represented by the same branch in the $\|\psi\|_2$ bifurcation diagram), reported in Fig. 3 for $Re = 15.8$. The symmetries linking the four states are the π -vertical shift $t_2(\psi(x, y)) = \psi(x, y + \pi)$ (one thus obtains states 3 and 4 from 1 and 2, respectively) and the transformation $\mathcal{T}_\pi \mathcal{B}\psi(x, y) = -\psi(x + \pi, -y)$, with $\mathcal{T}_\pi \psi(x, y) = \psi(x + \pi, y)$ being the shift of π along the x -direction and $\mathcal{B}\psi(x, y) = -\psi(x, -y)$; this transformation links 2 and 4 to 1 and 3, respectively. These states are characterized by horizontal sinusoidally shaped stripes of alternating positive and negative vorticity: however,

one of these stripes is differentiated by the presence of a strong and large vortex (negative for states 1 and 3 and positive for states 2 and 4), which squeezes all

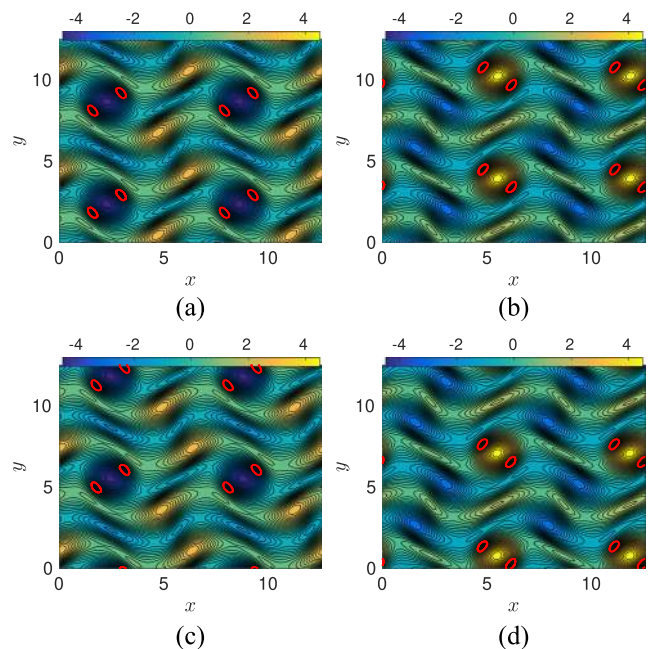


FIG. 3. The vorticity field for the four steady states when $Re = 15.8$. Bold red lines are contour levels of the vorticity distribution highlighting the maxima. (a) Steady state 1, $Re = 15.8$. (b) Steady state 2, $Re = 15.8$. (c) Steady state 3, $Re = 15.8$. (d) Steady state 4, $Re = 15.8$.

surrounding vortical structures giving rise to zones of strong vorticity gradients (dipoles) where most of the dissipation occurs; in Fig. 3, contour levels of palinstrophy distribution, identifying the maxima, are shown in bold red lines.

In panel (a) of Fig. 4, using the phase space of the mode $\hat{\psi}_{0,1}$, we represent all four states. Here we anticipate that, for all the subsequent Reynolds numbers until chaos, the dynamics will revolve around these four states, or states that are deformations of them: we shall in fact see oscillations close to each state, periodic transitions between them, until orbits that are the result of transitions, and oscillations of chaotic characteristics.

5. When $Re(S2, 0) = 16.4$, four simultaneous Hopf bifurcations appear. The resulting oscillatory solutions correspond, in the physical space, to localized oscillations of the vortex cores with a null mean drift velocity. In panels (a) and (b) of Fig. 2, one can see, at $Re = 16.95$, periodic oscillations of the L^2 -norm of ψ . In panels (a) and (b) of Fig. 4, we report, in the phase space of the mode $\hat{\psi}_{0,1}$, four periodic orbits encircling the steady state solutions.
6. When $16.96 < Re < 17.3$ (in Fig. 1, between S3 and S4), the solution switches randomly between these orbits. The merging (*gluing*) of the orbits has not stabilized yet. The physical behavior of the fluid during this process is a transition between states that are deformations of the four steady solutions represented in Fig. 3, therefore giving rise to an apparent vertical and horizontal motions

of the vortical structure switching randomly its direction (see Fig. 2). The transition phenomenon is clearly visible in the phase space, see panel (c) of Fig. 4, and is called *gluing bifurcation*.

7. At point S4, when $Re = 17.3$, the merging stabilizes, the random switching disappears, and the system settles to a periodic oscillation with a bulk vertical drift (both upward and downward motion solutions are allowed) and null horizontal mean velocity. The vertical drift is detectable from the phase portrait of $\hat{\psi}_{0,1}$ in panel (d) of Fig. 4 when $Re = 17.4$ and in panel (e) when $Re = 21.3$.

For higher Re , two branches are present each one leading to chaotic states. We shall describe these two different branches separately.

A. Route to chaos in the upper branch

The upper branch, which has already been described in detail,⁶ is characterized by drifting and oscillating solutions [denoted, in panel (c) of Fig. 1, with the red solid squares between points D3 and D4] that eventually become chaotic; this route is characterized by the features typical of the *Pomeau-Manneville* scenario, where transition to chaos is due to intermittency.

- (a) In D3, at $Re(D3, 0) = 17.8$, one can observe the appearance of coexisting (with the periodic orbit we denoted with black inverted triangles) stable drifting states. These states have the same symmetries and properties observed between D1 and D2.

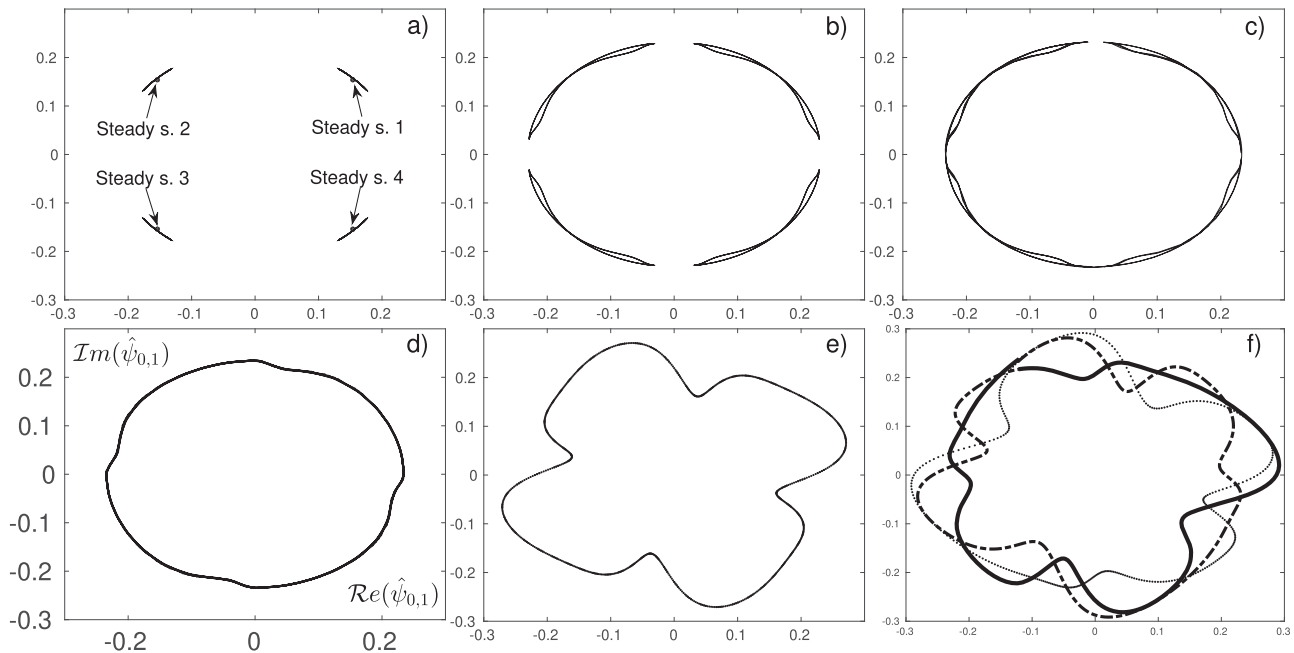


FIG. 4. Phase portraits and trajectories of $(Re(\hat{\psi}_{0,1}), Im(\hat{\psi}_{0,1}))$ on the branch with horizontally steady solutions. From (a) to (f), the Reynolds number is $Re = 15.8/16.42, 16.96, 16.98, 17.4, 21.3, 21.8$. In (a), the black bold points stand for the four steady states when $Re = 15.8$, while the closed curves stand for the four Hopf states when $Re = 16.42$.

- (b) In D4, at $Re(D4, 0) = 22$, the four traveling solutions bifurcate simultaneously to a drift-and-oscillate state. In Fig. 2, we plot the L^2 -norm of ψ for the drifting and drift-and-oscillate solutions, at $Re = 21.2$ and 24 , respectively.
- (c) When $Re > 25.7$, after D5, the flow becomes chaotic (as one can see with a Lyapunov exponent analysis^{40,50}) via intermittent bursts between unstable recurrent motions.

B. Route to chaos in the lower branch

The route to chaos in the lower branch departing from the steady states, on the other hand, has not been extensively studied, and we shall therefore give a more detailed description, especially for the new upcoming states.

The lower branch begins with solutions that, in panel (c) of Fig. 1, are denoted by black inverted triangles. Between points S4 and S5, as we already mentioned, these solutions translate vertically while pulsating. Subsequent bifurcations are the following:

- (A) At $Re = 21.35$, in S5, the state (black inverted triangles) loses its stability through a bifurcation that was left unnoticed in the previous literature: it is a *period-tripling* bifurcation. In panel (f) of Fig. 4, the period-tripling of the phase portrait is evident. The presence of this bifurcation is also visible in the time spectrum $\alpha_\nu(t)$ of $\|\psi\|_2$, where it appears an excited frequency $\bar{\nu}_{3T}$ which is 1/3 of the frequency $\bar{\nu}_{gH}$ of the glued state. This excited mode is shown in Fig. 5(b) when $Re = 21.946$. In panels (a) and (b) of Fig. 2, we can see, at $Re = 21.3557$, $\|\psi\|_2$ for the period-tripled state, while, on the right side of Fig. 6, we report the oscillation period T of all the periodic states (notice the presence of a gap for $16.96 \leq Re \leq 17.3$ because of the random switching related

to the gluing bifurcation). At $Re(S5, 0) = 21.35$, one can see the jump related to period-tripling in both $\|\psi\|_2$ and physical solution.

A typical behavior of the flow is depicted in Fig. 7, panels (a) to (f), where, for $Re = 21.6$, we show the contours of the vorticity during a whole period of $\|\psi\|_2$ starting from $t = 30.86$. The various times correspond to the extrema of the palinstrophy, see panel (g), when vorticity gradients are at their peaks or to their lowest. Notice how the vorticity field passes through states that are still reminiscent of the steady states reported in Fig. 3: At $t = 30.86$, one can recognize the structure of the steady state 3, while subsequent maxima of palinstrophy are similar to the other steady states (in the order: $2 \rightarrow 1 \rightarrow 4$). During the time evolution, the fluid experiences various rearrangements of the large eddies, with a strengthening and weakening of the dipolar structures which are faster compared to the glued state case. From $t = 30.86$ to $t = 31.87$, the negative core of vorticity initially centered close to $\approx(2, 5.7)$ weakens, while the positive core in $\approx(5.1, 3.8)$ becomes stronger. This core reaches its maximum intensity at $t \approx 31.95$, when \mathcal{P} has another peak, and forms the dipolar-like structure together with the negative core below it and visible in (c). In the same panel, the contour levels of the maximum palinstrophy distribution are shown in bold red, and they are localized in the middle of the dipolar structures. The other relevant region of high palinstrophy is in correspondence with another dipolar structure made of a negative core and a smaller positive core. The subsequent phase of decreasing \mathcal{P} and \mathcal{E} up to $t \approx 32.4$ is characterized by the weakening of these cores. From $t = 32.47$ up to $t = 33.61$, \mathcal{P} increases its value up to its maximum, and the periodic structure composed by the positive and negative cores centered in $\approx(5.2, 7.3)$ and $\approx(5.9, 5.8)$ is visible in (f). All phases of increasing/decreasing \mathcal{P} and \mathcal{E} are therefore a signature of the rearrangement of paired vorticity

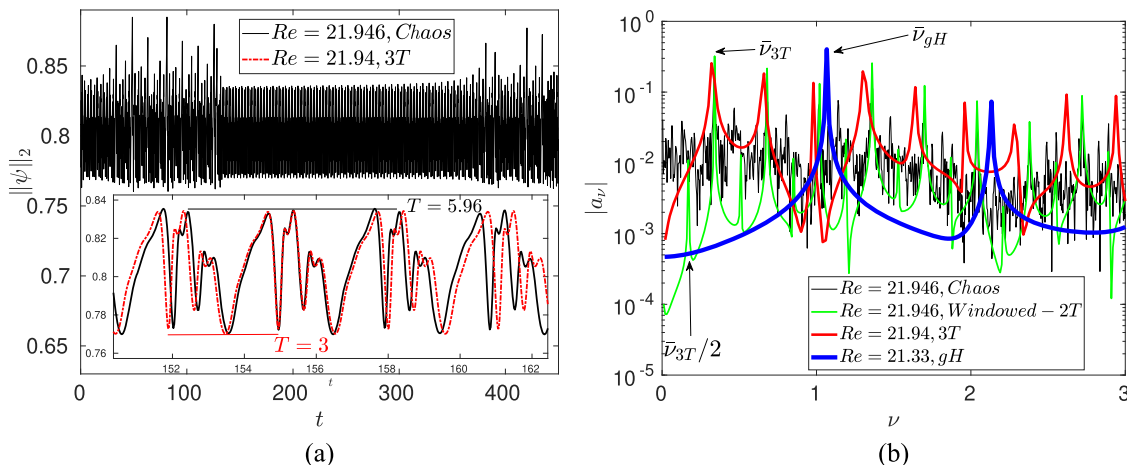


FIG. 5. (a) Time evolution of $\|\psi\|_2$ for the chaotic state when $Re = 21.946$, $Ri = 0$. In the inset, the time evolution is shown for a time interval when the period-doubling appears, and we superpose the time evolution of $\|\psi\|_2$ for the period-tripling state (dashed-dotted red line) when $Re = 21.94$. (b) Time spectrum, in lin-log scale, of $\|\psi\|_2$ for the chaotic state when $Re = 21.946$, $Ri = 0$. Superposed the time spectrum of the window between $t = 160$ and $t = 250$ (green), the time spectrum for the period-tripling state (red) when $Re = 21.946$, and the glued state (blue) when $Re = 21.33$.

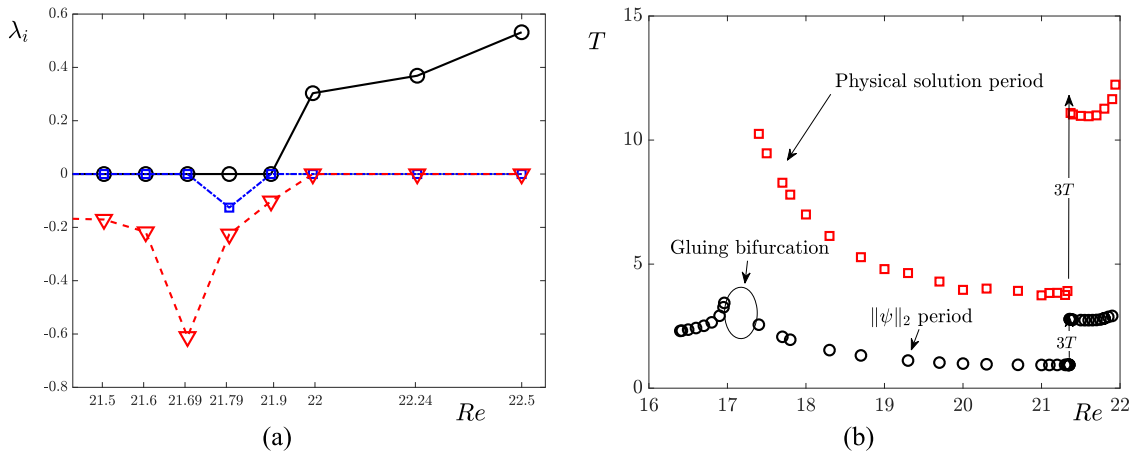


FIG. 6. The left panel reports the behavior of the Lyapunov exponents $\lambda_1 > \lambda_2 > \lambda_3$ (marked, respectively, with black empty circles, blue empty squares, red inverted triangles) as functions of Re in the lower branch of the bifurcation diagram [see panel (c) of Fig. 1]. The right panel reports the oscillation period $T(Re)$ for horizontally steady solutions. We compute it from $\|\psi\|_2$ (black empty circles) and from the physical solution (red empty squares).

cores of opposite sign. We also notice that the growth of \mathcal{P} and \mathcal{E} is generally anticipated by the growth of the kinetic energy input rate \mathcal{F} , as one can see in panel (g): the growth of \mathcal{F} leads

to a momentaneous accumulation of kinetic energy (in regions where the vorticity cores strengthen), which is then dissipated by the consequent high gradients.

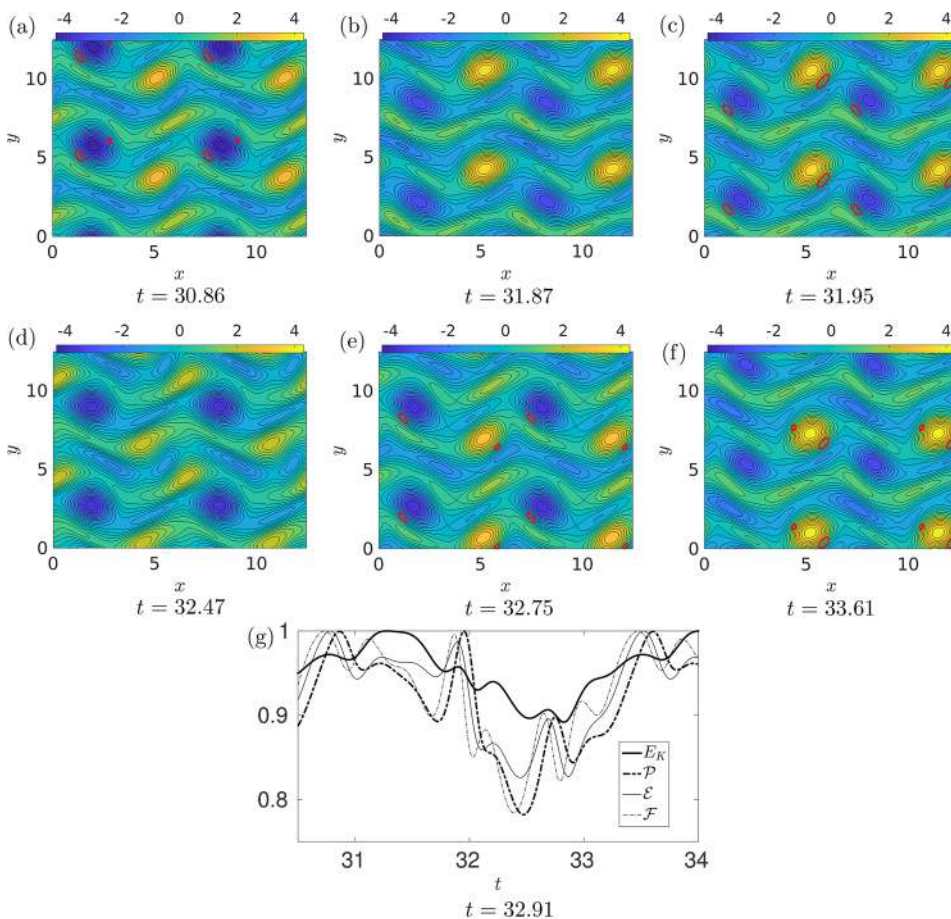


FIG. 7. [(a)–(f)] The vorticity field for $Re = 21.6$, period-tripled state, at different times corresponding to the peaks of the palinstrophy. Bold red lines are contour levels of the palinstrophy distribution highlighting the maxima. (g) Time evolution of energy E_K , enstrophy \mathcal{E} , palinstrophy \mathcal{P} , and energy growth rate \mathcal{F} (all quantities are rescaled with their maxima: $\max E_K = 0.3453$, $\max \mathcal{E} = 1.5450$, $\max \mathcal{P} = 6.2675$, $\max \mathcal{F} = 1.5500$).

(B) Finally, at $Re(S6, 0) = 21.945$, the period-tripled state loses its stability and the system settles to a chaotic regime, denoted by (blue stars) in Fig. 1. We have computed the Lyapunov exponents on this branch, and in panel (a) of Fig. 6, we show the three largest exponents for Re across $S6$. We see that after $Re = 21.945$ one of the exponents becomes positive indicating the solution to be chaotic. The description of the flow evolution in terms of \mathcal{P} growth phases is very similar to the one performed for the period tripled state, although in this case \mathcal{P} (and also $E_R, \mathcal{E}, \mathcal{F}$) varies in a non-regular way, and the differences between the maxima and the minima of \mathcal{P} are larger than those in the previous tripled state. This means that the dipolar structures pass more rapidly between phases of stronger and lower intensity.

Despite this chaotic behavior in the solution, we notice that for Re slightly above $Re(S6, 0)$ the chaotic regime is actually characterized by the presence of regular behavior in specific time windows. In particular, a *period doubling* state alternates in time with a chaotic state. This can be deduced from the time evolution of $\|\psi\|_2$ for $Re = 21.946$ in Fig. 5(a) where, in the window $150 \lesssim t \lesssim 300$, the solution undergoes a period doubling of the previous period-tripled state: in (b), the time spectrum of $\|\psi\|_2$ in this window shows the presence of an excited mode in correspondence with a frequency which is half of the frequency $\hat{\nu}_{3T}$ of the period-tripled state.

However, period-doubling alternates randomly with phases of chaos. In Fig. 5(b), the appearance of time frequencies in the whole spectrum is another signature of the system chaotic behavior, Fig. 5(a).

As we shall see in the weak stratification case ($Ri = 0.001$), the transition to the chaotic regime in this branch is more regular, in the sense that, after the period tripling, a sequence

of other period doubling/tripling bifurcations appears before the chaotic state formation.

IV. WEAKLY STRATIFIED KOLMOGOROV FLOW

In Secs. III A and III B, we have reviewed the set of transitions leading the Kolmogorov flow to chaotic states. In this section, we shall introduce a temperature gradient across the vertical y direction. We shall see that the introduction of stratification leads to the appearance of a variety of states not present in the non-stratified fluid. We shall present our results, first fixing the value of Ri and then investigating the dynamics of the transitions for $0 < Re < 30$. In this paper, we shall give a detailed account only for values of $0 < Ri \leq 5 \times 10^{-3}$, as for higher Ri preliminary inspections showed new dynamics that we believe deserve a separate analysis.

When the stratification values are $Ri \leq 10^{-4}$, our simulations have revealed no significant change with respect to the case $Ri = 0$. In fact, when $Ri \leq 10^{-4}$, the presence of the temperature gradient does not change neither the bifurcation points nor the qualitative characteristics of the states that we have seen for the non-stratified fluid; the effect of the stratification reveals itself only from the fact that some of the bifurcation points are slightly shifted in the Reynolds number. To be more precise: the bifurcation points $P1, D1, D2,$ and $S1$, appearing in the bifurcation diagram at low Re , remain the same (or, at least, their shift is not noticeable), while the bifurcation points appearing for larger Re are slightly shifted. In Table I, the bifurcation points of the non-stratified and the stratified flows are compared. For $Ri \leq 10^{-4}$, one can see that the bifurcation points are very similar: the most relevant features are as follows: first, the overall tendency of the temperature gradient to reduce the range of values in which the horizontal drifting solutions exist (the intervals $D1D2$ and

TABLE I. Bifurcation points of the non-stratified and stratified ($Ri = 10^{-4}, 10^{-3}$ and 5×10^{-3}) Kolmogorov flow.

	$Ri = 0$	$Ri = 10^{-4}$	$Ri = 10^{-3}$	$Ri = 5 \times 10^{-3}$
P1	$5/\sqrt{6}$...	2.055 ± 0.005	2.058 ± 0.005
D1	8.3	...	8.43 ± 0.03	8.85 ± 0.05
D2	15.8	...	15.35 ± 0.05	13.65 ± 0.05
D3	17.8	17.87 ± 0.02	18.45 ± 0.05	21.1915 ± 0.0005
D4	22	21.9 ± 0.1	22.03 ± 0.03	23.85 ± 0.05
D5	25.7	25.68 ± 0.01	25.055 ± 0.005	25.155 ± 0.005
S1	15.2	...	14.7 ± 0.1	13.55 ± 0.05
S2	16.4	16.32 ± 0.02	15.95 ± 0.05	14.15 ± 0.05
S3	16.96	16.91 ± 0.01	16.49 ± 0.01	14.15 ± 0.05
S4	17.3	17.25 ± 0.05	17.31 ± 0.01	14.743 ± 0.003
S4 _c	17.3	17.25 ± 0.05	17.31 ± 0.01	15.33 ± 0.01
S4' _c	17.3	17.25 ± 0.05	17.31 ± 0.01	19.13 ± 0.03
S4''	17.3	17.25 ± 0.05	22.3995 ± 0.0005	21.65 ± 0.05
S4'''	17.3	17.25 ± 0.05	22.3995 ± 0.0005	23.73 ± 0.03
S5	21.35	21.43 ± 0.01	21.9555 ± 0.0005	24.4045 ± 0.0005
S6'	21.35	21.43 ± 0.01	22.2835 ± 0.0005	24.623 ± 0.003
S6''	21.35	21.43 ± 0.01	22.3245 ± 0.0005	24.658 ± 0.002
S6'''	21.35	21.43 ± 0.01	22.3335 ± 0.0005	24.6665 ± 0.0005
S6	21.945	21.985 ± 0.005	22.3365 ± 0.0005	24.6685 ± 0.0005

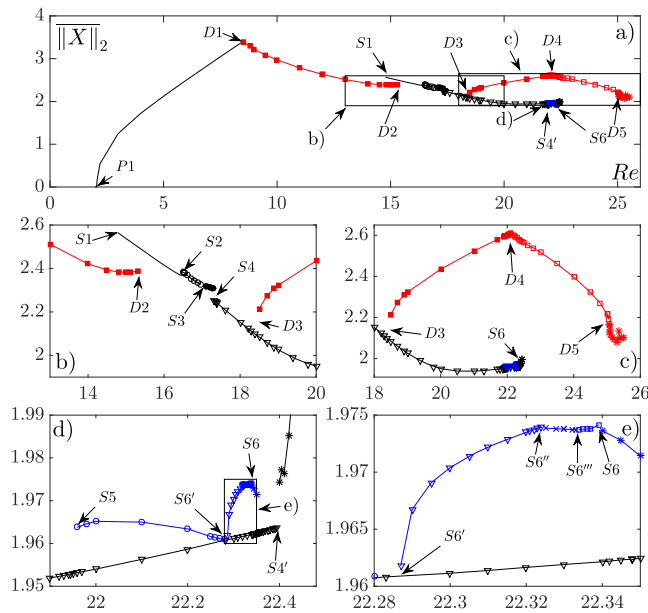


FIG. 8. Bifurcation diagram of the stratified Kolmogorov flow when $Ri = 10^{-3}$ and $Pr = 1$. The panels are progressive magnifications of the diagram. The points are the temporal mean of $\|X\|_2$ [defined in (10)] for each numerical solution. Refer Fig. 1 for symbol legend. Here black asterisks denote the chaotic transition of the glued state. The subcritical period-tripling bifurcation is denoted with blue empty circles. Blue inverted triangles, blue crosses, and blue empty squares denote the period-doubling bifurcations, and the blue asterisk denotes its chaotic bifurcation.

D3D4) and second to advance the appearance of the steady, oscillating, and glued-oscillating solutions.

When $Ri = 10^{-3}$, we can observe the same tendency of reducing the region where the horizontal drift exists, with the tendency to force toward a steady solution (from D1 to S1). However, when the steady solution disappears, new

transitions and new interesting phenomena are observed; this will be the subject of Sec. IV A.

A. Steady and drifting states for $Ri = 0.001$

When we induce a temperature stratification such that $Ri = 10^{-3}$, the route to chaos is modified by the appearance of new states. From Fig. 8, we see that the overall structure of the bifurcations and the states typical of the non-stratified Kolmogorov flow are left unchanged; however, we shall see how the route to chaos departing from the steady solution has now a more complex structure. Looking at Table I, one sees that, as we expect from the stabilizing nature of the temperature gradient, the laminar state bifurcates for Re larger than $5/\sqrt{6}$; the newly formed steady state, see Fig. 9, has the same structure that we have seen for the non-stratified fluid: two superposed dipoles along the vertical direction. Solutions belonging to this branch have the symmetries $\mathcal{T}_\pi \mathcal{A}(\psi(x, y), \theta(x, y)) = (\psi(-x + \pi, -y + \pi/2), \theta(-x + \pi, -y + \pi/2))$, $\mathcal{T}_\pi \mathcal{B}(\psi(x, y), \theta(x, y)) = (-\psi(x + \pi, -y), -\theta(x + \pi, -y))$, and $t_2(\psi(x, y), \theta(x, y)) = (\psi(x, y + \pi), \theta(x, y + \pi))$, where $\mathcal{A}(\psi(x, y), \theta(x, y)) = (\psi(-x, -y + \pi/2), -\theta(-x, -y + \pi/2))$ represents the combination of a reflection in the (x, y) -plane with the vertical shift of half of the wavelength of the forcing function; $\mathcal{B}(\psi(x, y), \theta(x, y)) = (-\psi(x, -y), -\theta(x, -y))$ is the rotation of π in the (y, ψ, θ) -plane; and finally $t_2(\psi(x, y), \theta(x, y)) = (\psi(x, y + \pi), \theta(x, y + \pi))$ and $\mathcal{T}_\pi(\psi(x, y), \theta(x, y)) = (\psi(x + \pi, y), \theta(x + \pi, y))$ are, respectively, the vertical and horizontal shifts of π . The right panel of Fig. 9 shows the temperature variations from the linear temperature gradient. The highest and lowest temperature deviations appear to be concentrated in the circulating region between the vortices.

The steady state loses its stability in D1 (from which the drifting state branch departs) for a Re which is higher compared to the non-stratified fluid, i.e., $Re(D1, 10^{-3}) > Re(D1, 0)$. One can see that the basic mechanism of this drift bifurcation is a subharmonic instability, which occurs when the second harmonic of the basic pattern is not damped enough.⁵¹ The presence of the stratification, which adds a further damping mechanism to the fluid viscosity, is able to postpone

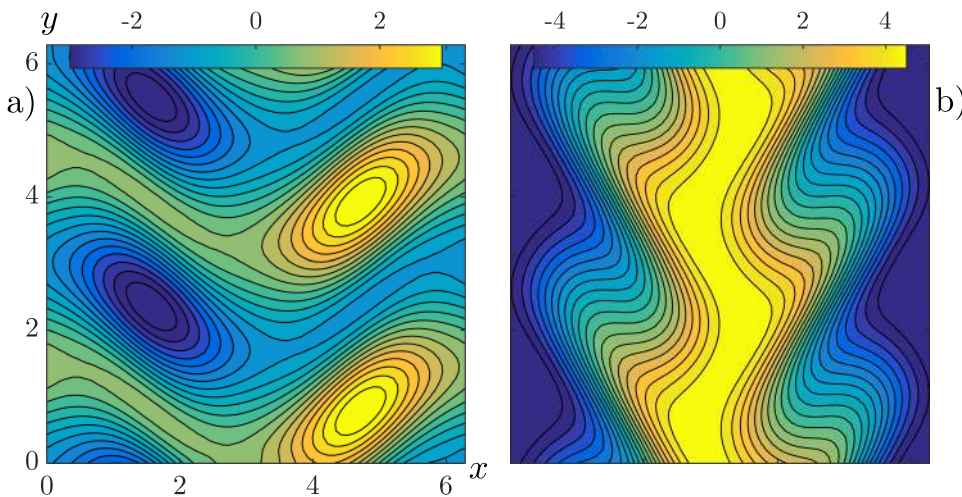


FIG. 9. Steady state solution when $Re = 8.4$, $Ri = 10^{-3}$, and $Pr = 1$. Vorticity is in the left panel and temperature variations on the right.

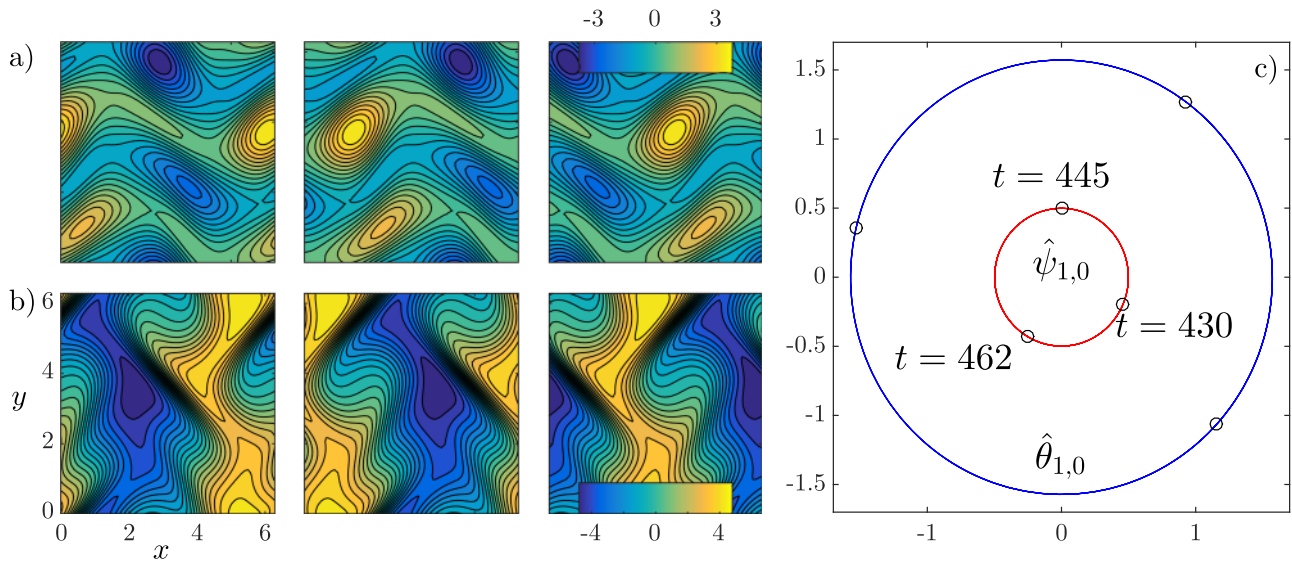


FIG. 10. Time evolution of the drifting state where $Re = 12$, $Ri = 10^{-3}$, and $Pr = 1$. Panels (a) and (b) are for vorticity and temperature, respectively. Over a period length, these are snapshots taken at $t = 430, 445, 462$. Real and imaginary parts of the mode $(1, 0)$ are shown in panel (c) for both stream function and temperature.

the appearance of this bifurcation. This implies that when Re is slightly above $Re(D1, 10^{-3})$, the drifting is much faster for the non-stratified flow. On the other hand, once the drifting behavior has already established, the additional nonlinear subharmonic interactions with the temperature are able to make faster the drifting behavior. In fact, at $Re = 12$ well after the drifting bifurcation, computing the period $T_{Ri=10^{-3}}$ of the drifting state D1, one finds that stratification makes

it smaller so that the drift is significantly faster for higher Ri . For instance, at $Re = 12$, $T_{Ri=5 \times 10^{-3}} \approx 49, T_{Ri=10^{-3}} \approx 55, T_{Ri=0} \approx 60$.

In panel (c) of Fig. 10, we show the phase portrait in the complex plane of the Fourier modes $\hat{\psi}_{1,0}$ (which is the subharmonic of the main period) and $\hat{\theta}_{1,0}$. We can see the oscillatory behavior of the components around the origin which is typical of the drifting behavior.⁵¹ The drifting structure can be seen

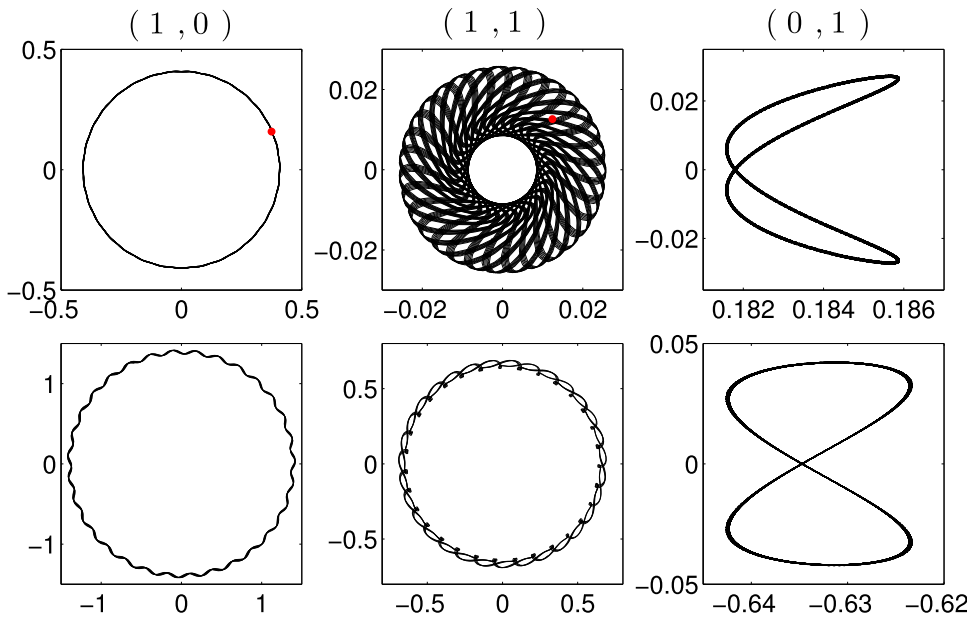


FIG. 11. Oscillating drifting solution when $Re = 22.35$, $Ri = 10^{-3}$, and $Pr = 1$. Phase portraits of modes $k = (1, 0), (1, 1)$, and $(0, 1)$: the axes are the real and imaginary parts of $\hat{\psi}_k$ for the top panels and $\hat{\theta}_k$ for the bottom panels.

in panels (a) and (b) where, for $Re = 12$, we show the vorticity and the temperature, respectively, at times $t = 430, t = 445$, and $t = 462$.

In the non-stratified fluid, the drifting state branch becomes unstable in the window $Re(D2, 0) < Re < Re(D3, 0)$; for $Ri = 10^{-3}$, this region becomes significantly broader; see Table I. From $Re(D3, 10^{-3})$, the drifting state regains its stability. It maintains the same symmetries as before the bifurcation $D2$ and in $D4$ undergoes a Hopf bifurcation. In Fig. 11, we can see how the oscillatory behavior mixes with the drifting behavior: there is a vertical oscillation due to mode $(0, 1)$; the

mode $(1, 0)$ behaves as for the purely drifting solution describing a circle centered in the origin, while mode $(1, 1)$ oscillates while drifting. We recall that for purely drifting solutions the mode $(0, 1)$ has a constant value, while the phase portrait of $(1, 0)$ is a circle.

The final bifurcation we observe on this branch is toward a chaotic attractor in $D5$, where the drifting-and-oscillating state, in presence of stratification, is destabilized earlier: $Re(D5, 10^{-3}) < Re(D5, 0)$. The chaotic state presents the intermittent feature typical of the non-stratified Kolmogorov flow.

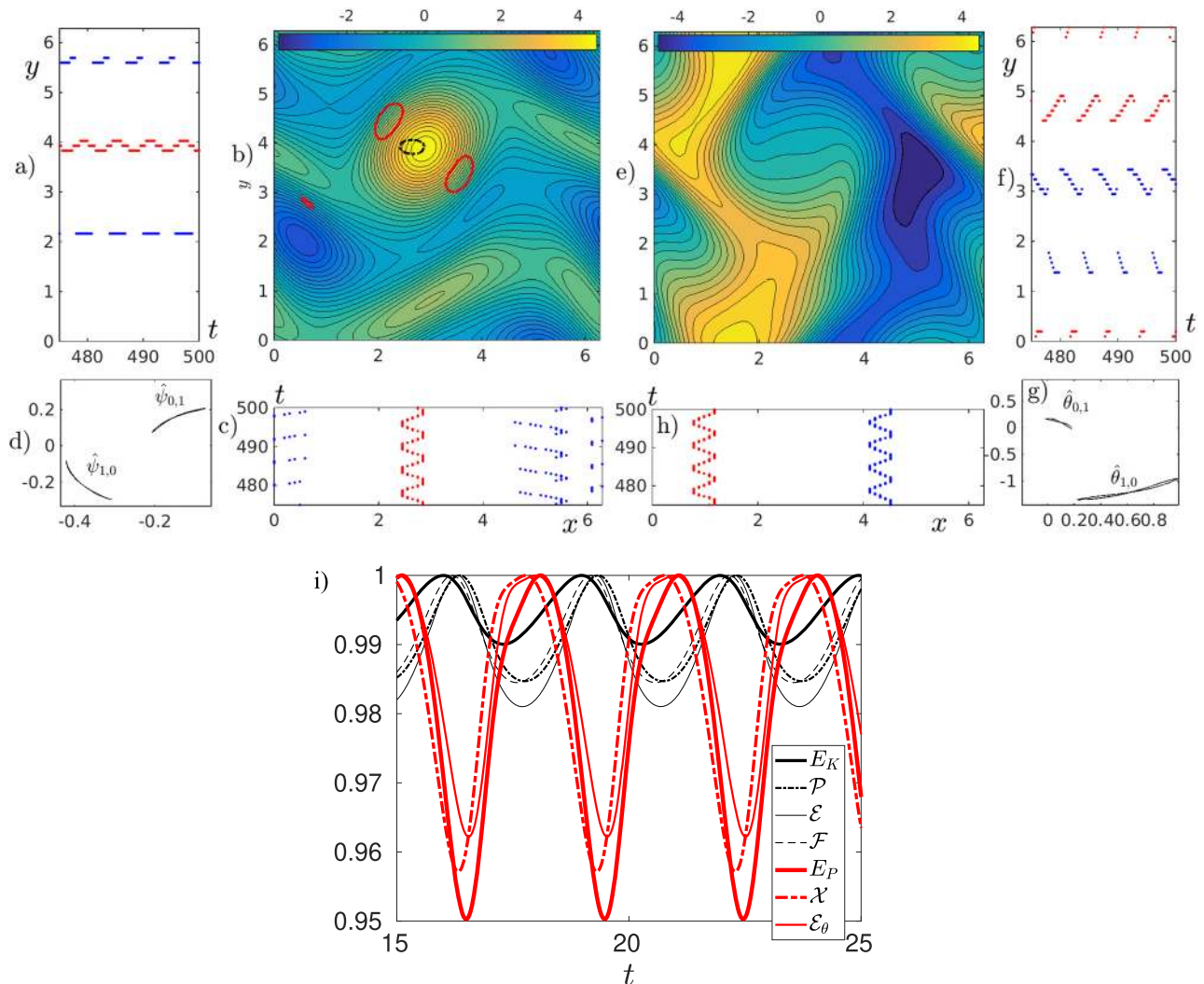


FIG. 12. Time evolution of the Hopf state when $Re = 16.3, Ri = 10^{-3}$, and $Pr = 1$. Contour plots in panels (b) and (e) are the vorticity and temperature. Times are related to the first maximum of the palinstrophy in (i). The dotted black line in (b) denotes the elliptic trajectory described by the center of the positive core. Bold red curves denote the contour levels of the highest palinstrophy distribution. Panels (a) and (c) report the temporal position of the vorticity extrema, while panels (f) and (h) are for temperature: red dots denote maxima and blue dots denote minima positions. The phase portrait of the real and imaginary parts of $\hat{\psi}_k$ and $\hat{\theta}_k$ for $k = (1, 0), (0, 1)$ is shown, respectively, in panels (d) and (g). (i) Time evolution of kinetic energy E_K , enstrophy \mathcal{P} , palinstrophy \mathcal{E} , kinetic energy growth rate \mathcal{F} , potential energy E_P , and exchange rate \mathcal{X} (all quantities are rescaled with their maximum: $\max E_K = 0.3763, \max \mathcal{E} = 1.6756, \max \mathcal{P} = 6.7523, \max \mathcal{F} = 1.6896, \max E_P = 0.0032, \max \mathcal{X} = 0.0173, \max \mathcal{E}_\theta = 0.0178$). Multimedia view: <https://doi.org/10.1063/1.5081105.1>

B. Hopf bifurcation, glued states, and period-tripling for $Ri = 0.001$

Now we consider the steady state that becomes stable in S1 (see Fig. 8). The main differences introduced by stratification are on this branch and on its transitions. For this increased Richardson number, as mentioned above, the stability region of the drifting branch shrinks. On the other hand, the size of the stability region of the steady branch is left unchanged, but the appearance of S1 is significantly anticipated by stratification, while the steady state bifurcates for $Re(S2, 10^{-3}) < Re(S2, 0)$. After this, it follows the series of periodic orbit bifurcations similar to what we have seen for the non-stratified fluid. In the following, we describe (i) the

flow for $Re = 16.3$ following the Hopf bifurcation at S2 for $Re(S2, 10^{-3}) \approx 15.95$, (ii) a gluing bifurcation at $Re = 16.9$, and (iii) a glued periodic orbit for $Re = 21.96$.

The Hopf states present localized oscillations which are shown in Fig. 12 (Multimedia view). In panels (a) and (c) [in panels (f) and (h)] is reported the temporal position of the extrema of the means for vorticity (for temperature), while the contour plots are in panel (b) for vorticity and in panel (e) for temperature. Oscillations can be deduced from the physical trajectories of the streamwise and spanwise components of the extrema over a whole time period. The period T_{Ri} of the Hopf states is larger as compared to the non-stratified case (for instance, $T_{Ri=10^{-3}} \approx 6.6, T_{Ri=10^{-4}} \approx 5.25, T_{Ri=0} \approx 4.65$ for $Re = 16.42$), which is an effect of the increased dissipation. The

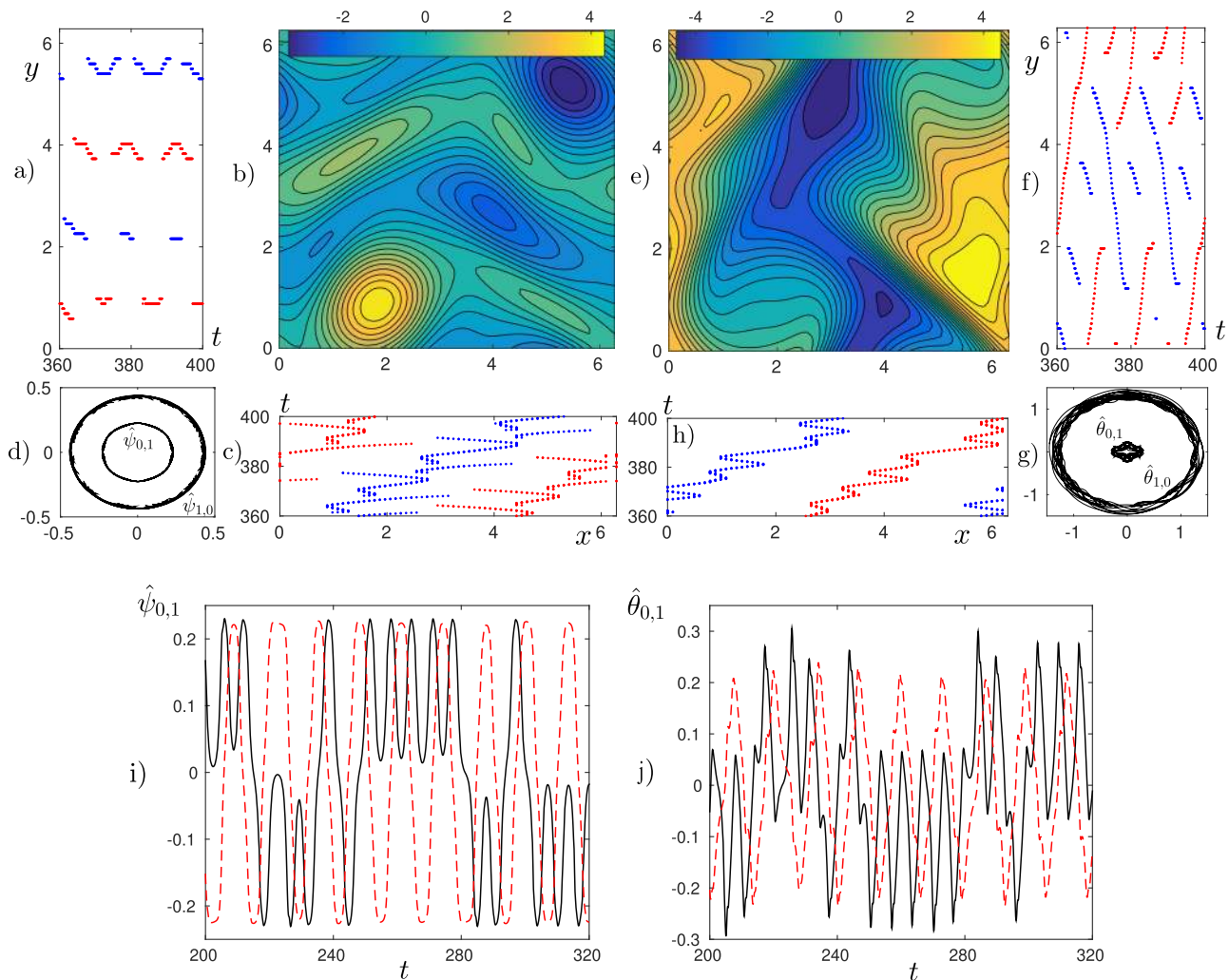


FIG. 13. Time evolution of the glued periodic orbit when $Re = 16.9, Ri = 10^{-3}$, and $Pr = 1$. Contour plots represent vorticity solutions in panel (b) and temperature in panel (e). The temporal position of the extrema of the mean fields is reported in (a) and (c) for vorticity and (f) and (h) for temperature. Red dots stand for maxima, and blue dots stand for minima. The phase portrait of the real and imaginary parts of $\hat{\psi}_{\mathbf{k}}$ and $\hat{\theta}_{\mathbf{k}}$ for $\mathbf{k} = (1, 0), (0, 1)$ is shown, respectively, in (d) and (g). In panels (i) and (j), there are the trajectories of the real (solid black line) and imaginary (dashed red line) parts of $\hat{\psi}_{0,1}$ and $\hat{\theta}_{0,1}$.

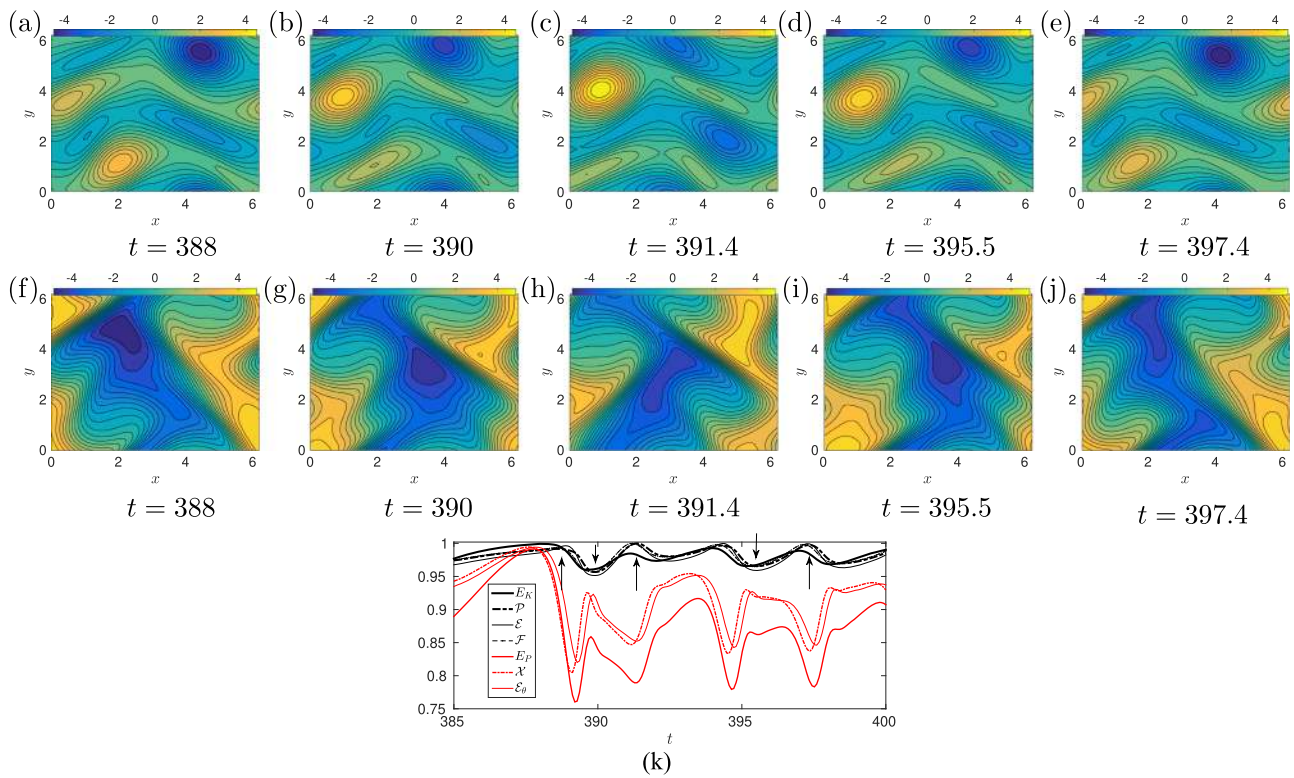


FIG. 14. [(a)–(e)] The vorticity ω and [(f)–(j)] the temperature variation θ , for the glued periodic orbit when $Re = 16.9$ and $Ri = 10^{-3}$. Times are related to relevant peaks of palinstrophy [signed with arrows in (k)]. (k) Time evolution of kinetic energy E_K , enstrophy \mathcal{E} , palinstrophy \mathcal{P} , kinetic energy growth rate \mathcal{F} , potential energy E_P , and exchange rate \mathcal{X} (all quantities are rescaled with their maximum: $\max E_K = 0.3759$, $\max \mathcal{E} = 1.6576$, $\max \mathcal{P} = 6.6682$, $\max \mathcal{F} = 1.6688$, $\max E_P = 0.0035$, $\max \mathcal{X} = 0.0182$, $\max \mathcal{E}_\theta = 0.0181$). Multimedia view: <https://doi.org/10.1063/1.5081105.2>

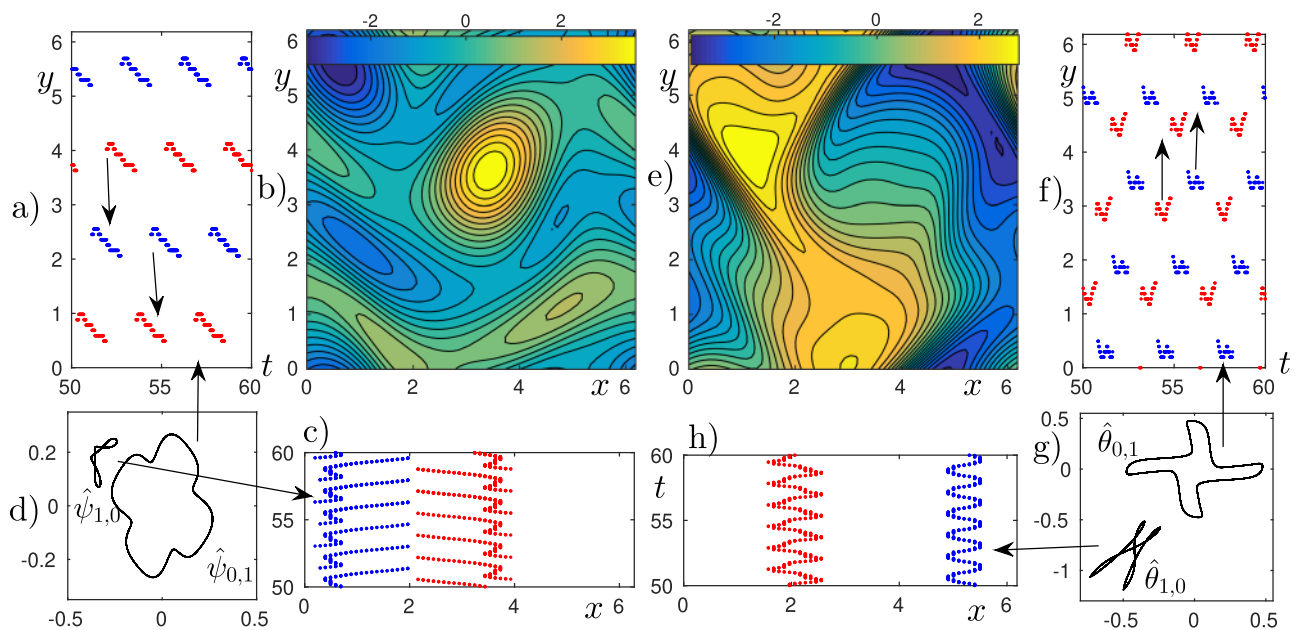


FIG. 15. Glued-state solution when $Re = 21.96$, $Ri = 10^{-3}$, and $Pr = 1$. Contour plots are (b) vorticity and (e) temperature. The time-evolution for the vertical and horizontal extrema are reported in (a) and (c) for vorticity and in panels (f) and (h) for temperature. Red dots stand for maxima, and blue dots stand for minima. The phase portrait of the real and imaginary parts of $\hat{\psi}_k$ and $\hat{\theta}_k$ for $k = (1, 0), (0, 1)$ are shown, respectively, in (d) and (g).

oscillating behavior is also evident from the phase plots in panels (d) and (g), where the modes $(1, 0)$ and $(0, 1)$ are localized in the phase plane for both stream function and temperature variations, and they follow trajectories that do not embed the origin. The typical structure of the vorticity [closely resembling the field seen in Fig. 3(b)] and temperature is shown in panels (b) and (e), with a main positive vortex core centered in $\approx(2.2, 4)$ which traces in time a small elliptic trajectory, the dotted black curve in figure, with a horizontal semi-axis larger than the vertical. When this core reaches the higher and

lower positions, see panel (a), it squeezes the smaller cores of opposite sign placed above on the left and below on the right, increasing the vorticity gradients and hence the palinstrophy of the flow; see panel (i). The relevant palinstrophy distribution contour levels are shown with the red curves, well visible between the above and below of the center of the positive core.

The oscillating states lose their stability through a gluing-bifurcation that occurs between S3 and S4; see Fig. 13. These states are characterized by an oscillating behavior of the

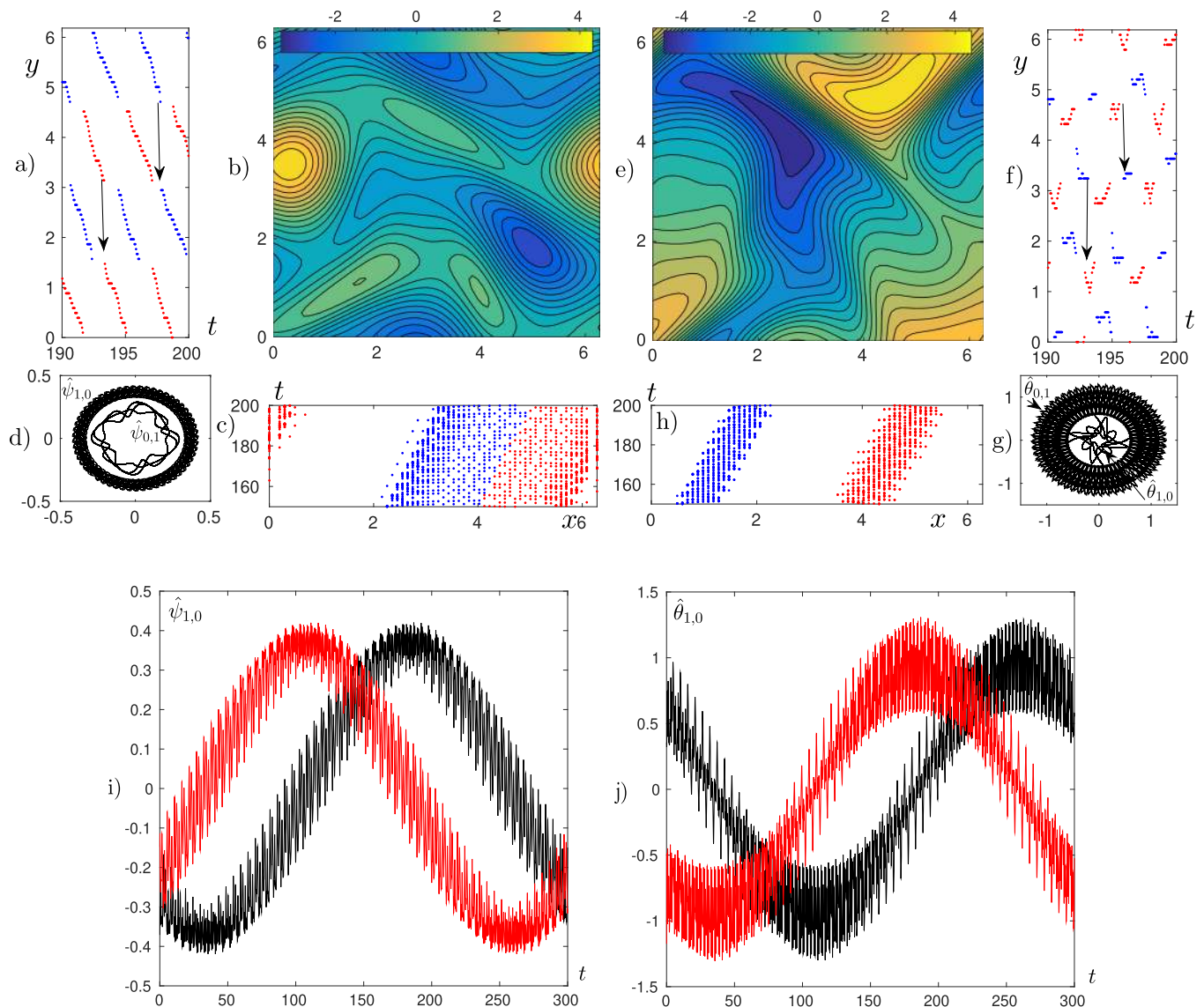


FIG. 16. Drift-and-oscillating solution when $Re = 22.287$, $Ri = 10^{-3}$, and $Pr = 1$. Contour plots are (b) vorticity and (e) temperature. The temporal position of the extrema of the means are reported in (a) and (c) for vorticity and (f) and (h) for temperature. Red dots stand for maxima, and blue dots stand for minima. The phase portrait of the real and imaginary parts of $\hat{\psi}_k$ and $\hat{\theta}_k$ for $k = (1, 0)$, $(0, 1)$ is shown, respectively, in (d) and (g). Panels (i) and (j) show the trajectories of the real and imaginary parts of mode $(1, 0)$ for the stream function and temperature over a drifting period.

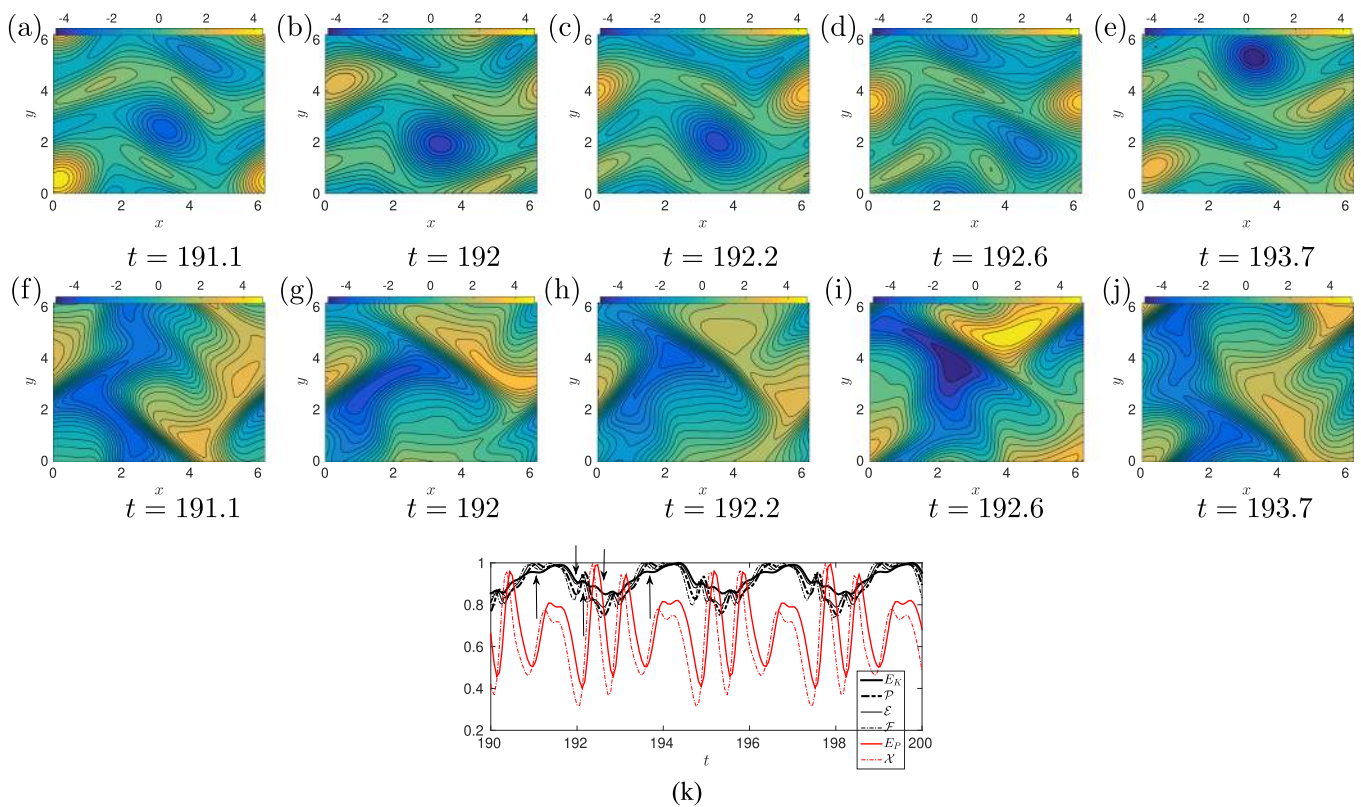


FIG. 17. [(a)–(e)] The vorticity ω and [(f)–(j)] the temperature variation θ , for the drift-and-oscillating solution when $Re = 22.287$ and $Ri = 10^{-3}$ at various time. (k) Time evolution of kinetic energy E_K , enstrophy \mathcal{E} , palinstrophy \mathcal{P} , kinetic energy growth rate \mathcal{F} , potential energy E_P , and exchange rate \mathcal{X} (all quantities are rescaled with their maximum: $\max E_K = 0.3420$, $\max \mathcal{E} = 1.5258$, $\max \mathcal{P} = 6.2159$, $\max \mathcal{F} = 1.5563$, $\max E_P = 0.0034$, $\max \mathcal{X} = 0.0228$). Times are related to relevant peaks of palinstrophy, signed with arrows in (k). Multimedia view: <https://doi.org/10.1063/1.5081105.3>

solution with alternating phases of strengthening and weakening of the vortical cores. These states present also a very slow drift superposed to a faster horizontal oscillation. These aspects can be inferred from the extrema trajectories of the main vortex cores and temperature variation in panels (c) and (f). Panels (d) and (g) show the above drifting motions with the phase portraits of the modes $\hat{\psi}_{1,0}$ and $\hat{\theta}_{0,1}$ embedding the origin. Strengthening and weakening of the cores are correlated to increasing and decreasing phases of E_K , \mathcal{E} , and \mathcal{P} , similar to the previous lower Re cases; however, the excursions of the energies and of dissipations are now much more pronounced [compare panel (k) of Fig. 14 (Multimedia view) with panel (i) of Fig. 12]; this is probably due to the fact that now the solution has to pass close to the four steady states and therefore has to go through intense phases of vortex reorganization. Vorticity and temperature evolution is reported in Fig. 14 (Multimedia view). From the evolution of the energy exchange rate \mathcal{X} , one can also observe how the transfer from kinetic to potential energy is less sustained during the phases of vortex core strengthening, as the larger part of the energy is used to reinforce the vorticity field. However one can observe that the transfer from kinetic to potential energy is always positive

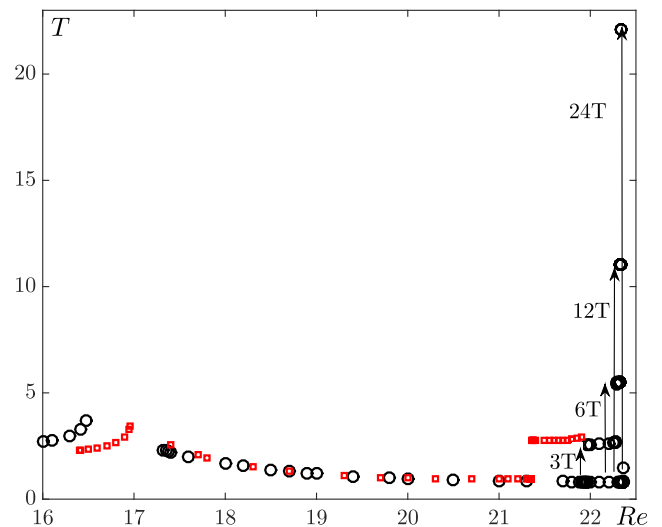


FIG. 18. Oscillation period (T) of the horizontally steady solutions versus the Reynolds number. Red empty squares stand for $Ri = 0$ and black empty circles for $Ri = 10^{-3}$.

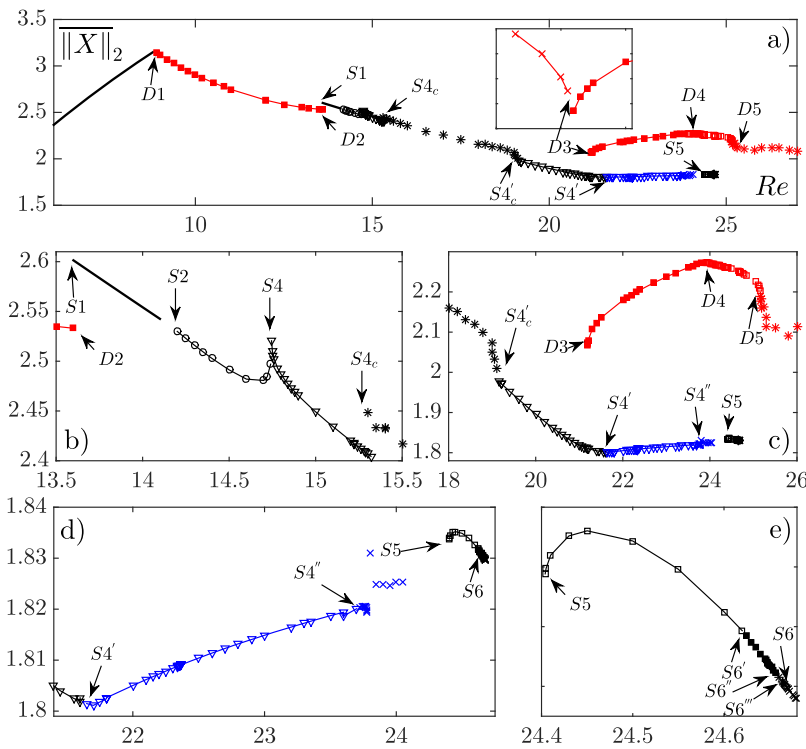


FIG. 19. Bifurcation diagram of the stratified Kolmogorov flow when $Ri = 5 \times 10^{-3}$ and $Pr = 1$. The insets are progressive magnifications of the diagram. The points are the temporal mean of $\|X\|_2$ [defined in (10)] for each numerical solution. Refer Fig. 1 for symbol legend. The blue branch contains period-tripled and period-doubled states.

and how the phases of sustained transfer are followed by an increase in thermal dissipation.

For the non-stratified fluid, after S_4 , the gluing process reaches a stable limit cycle which bifurcates supercritically in S_5 toward the period-tripled state. On the contrary, in the stratified case, the bifurcation in S_5 is subcritical and the glued state coexists with the period-tripled state branch until S_4' .

In Fig. 15, we show solutions for $Re = 21.96$, slightly after the period-tripling bifurcation S_5 but still on the branch of the glued state. The glued state persists until $Re(S_4', 10^{-3}) = 22.38$, where it reaches a chaotic state. When at S_5 the period-tripled state appears, the overall dynamics of the solution is similar to the glued solution, except that the cycle repeats itself after three times of the original period.

C. Transition to chaos for $Ri = 0.001$

The bifurcations departing from the period-tripled state branch [shown in panel (e) of Fig. 8] are one of the main differences from the non-stratified fluid: the transition toward the chaotic regime (which occurs between S_5 and chaotic bifurcation in S_6) occurs more slowly and has a richer structure.

In fact, the period-tripled state undergoes, in S_6' , a period-doubling bifurcation which is followed by two subsequent period-doubling bifurcations (in S_6'' and S_6'''). After this bifurcation, finally, the branch reaches the chaotic regime, which sets in at $Re(S_6, 10^{-3}) \approx 22.33 > Re(S_6, 0) \approx 21.92$.

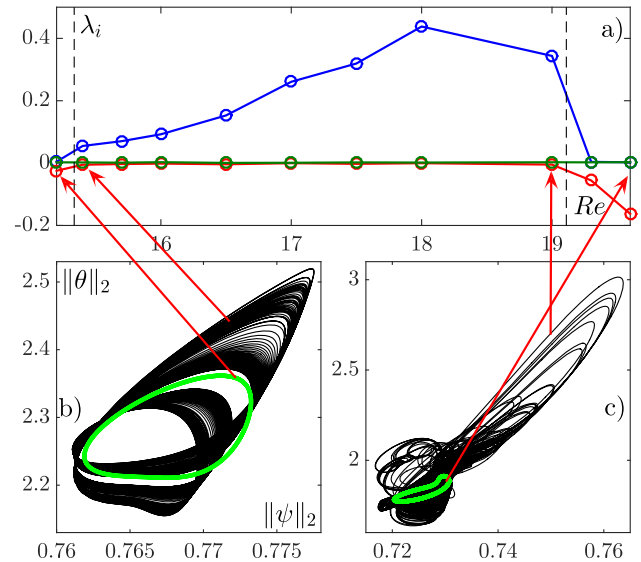


FIG. 20. Chaotic window inside the glued-state branch when $Ri = 0.005$. In panel (a), there are the three largest Lyapunov exponents $\lambda_1, \lambda_2,$ and λ_3 for solutions before and after the boundaries (marked as vertical dashed lines) of the chaotic window. In panels (b) and (c), we show the phase portrait in the plane of the vorticity and temperature's L^2 -norm. The black lines are for the solutions inside the chaotic window, and the green thick lines are for the stable solutions outside this region. In (b), we show norms for $Re = 15.2$ and 15.4 . In (c), $Re = 19$ and 19.6 .

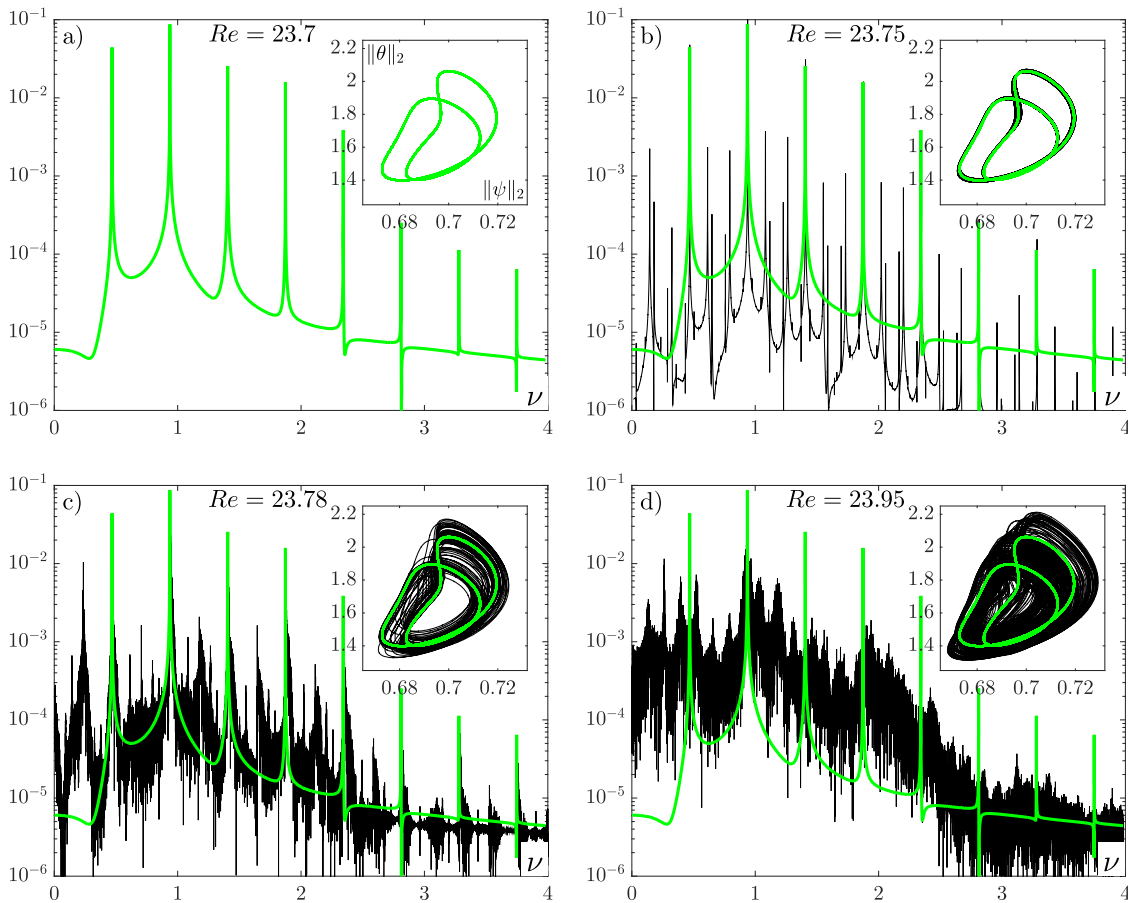


FIG. 21. In the four panels (a)–(d) we report the time spectra and (in the insets) the phase portraits of the solutions near the bifurcation to chaos $S4''$ of the period-doubling solution. The Reynolds numbers are $Re = 23.7, 23.75, 23.78,$ and 23.95 . In green we superpose the period-doubled solution of panel (a) as a reference.

As we can see in panels (d) and (g) of Fig. 16, the vertical wave vector $(0, 1)$ keeps the dynamics of the period-tripled state: it encloses the origin three times before repeating itself.

Before the bifurcation $S6'$, the horizontal mode $(1, 0)$ has a localized oscillation similar to those visible in panels (d) and (g) of Fig. 15. After the bifurcation in $S6'$, an overall horizontal drift superposes to the oscillation; indeed, the resulting phase portrait is a periodic oscillation around a circle centered in the origin—see panels (d) and (g) of Fig. 16. The (rightward) drift can be barely observed in Fig. 17 (Multimedia view) where vorticity and temperature variation are shown along with the energy evolutions. The horizontal drift has a long time periodicity which is not evident from the L^2 - norm of the system. In Fig. 18, we show the oscillation period T of the norm for periodic orbits belonging to the steady branch as a function of Re . We can clearly see the broadening of the steady state branch due to the stabilizing temperature stratification. As pointed out by the arrows, we see also the chain of period-tripling and three period-doubling bifurcations.

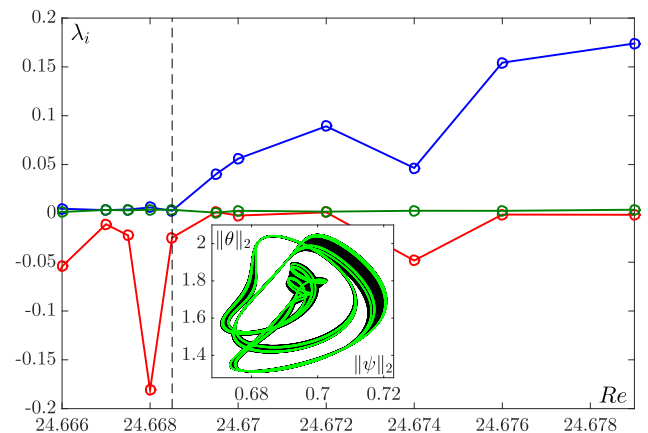


FIG. 22. Lyapunov exponents across the transition to chaos in $S6$ which is marked as a vertical dashed line. In the figure, are shown the three strongest exponents, and in the inset, we show the phase portrait in the $(\|\psi\|_2, \|\theta\|_2)$ -plane of the solution before ($Re = 24.6675$) and after ($Re = 24.6695$) $S6$.

D. $Ri = 0.005$

We now consider a higher Richardson number which is the highest value we consider in this work. Surveying simulations at $Ri = 0.01$ show a number of states not ascribable to the common Kolmogorov route to chaos, so we pick $Ri = 0.005$ which possesses the main structure of the non-stratified case but also introduces important variations to the route to chaos. Compared to the non-stratified fluid, the set of transitions has significant differences, but these mostly affect the branch departing from the steady states. In Fig. 19, we show the bifurcation diagram where we find bifurcations P1, D1, D2, S1, and S2 to be still present but shifted in the Reynolds number. The main differences lie in the gluing process, in the stability of the resulting glued state, in its bifurcation and subsequent route to chaos, and in the bifurcation point D3 of the horizontal drifting state branch.

As we may infer from Table I and Fig. 19, the first transitions are slightly shifted by stratification—larger Re are required to destabilize the laminar solution. The drifting state branch, lying between D1 and D2, has been shifted to higher Re and shortened in length, while the steady state branch departing from S1 appears at lower Re . We recall that for smaller Ri , the four steady state solutions undergo a Hopf bifurcation in S2, while a gluing bifurcation appears in S3 to finally settle to two periodic orbits in S4. When $Ri = 0.005$, the gluing process between S3 and S4 is suppressed [see panel (b) of

Fig. 19]—the four Hopf solutions abruptly merge to two glued states. From the same panel, we observe a completely new bifurcation in S4c. The glued state loses its stability, the solution becomes chaotic, and then the flow recovers its stability in S4c. We show in panel (a) of Fig. 20 the Lyapunov exponents of this chaotic window along this branch. We show the three largest exponents as a function of the Reynolds number and observe that $\lambda_i \leq 0$ everywhere except inside the window, where the largest exponent (λ_1) becomes positive, proving that these states are chaotic. In panels (b) and (c), we show the norm $\|\psi\|_2$ versus $\|\theta\|_2$ near the boundaries of the chaotic window where the stable solution is the green thick line and the chaotic solution is the black line.

When the glued state regains its stability in S4c, it persists until S4' where it shows another difference to the less stratified counterparts. Instead of bifurcating through a period-tripling, as in the previous cases, it shows a period-doubling bifurcation as we see in the inset of panel (a) in Fig. 21. This state persists until S4'' where it becomes chaotic as we can see in panels (b)–(d) on the same figure. Together with the phase portraits, we show the time spectra of $\|X\|_2$ highlighting the enrichment of frequencies as Re grows. The green lines in panels (b)–(d) mark the case of the stable period-doubled solution. As we see in panel (b), more subharmonics appear and when we look at (c) we see that the spectra have a lot

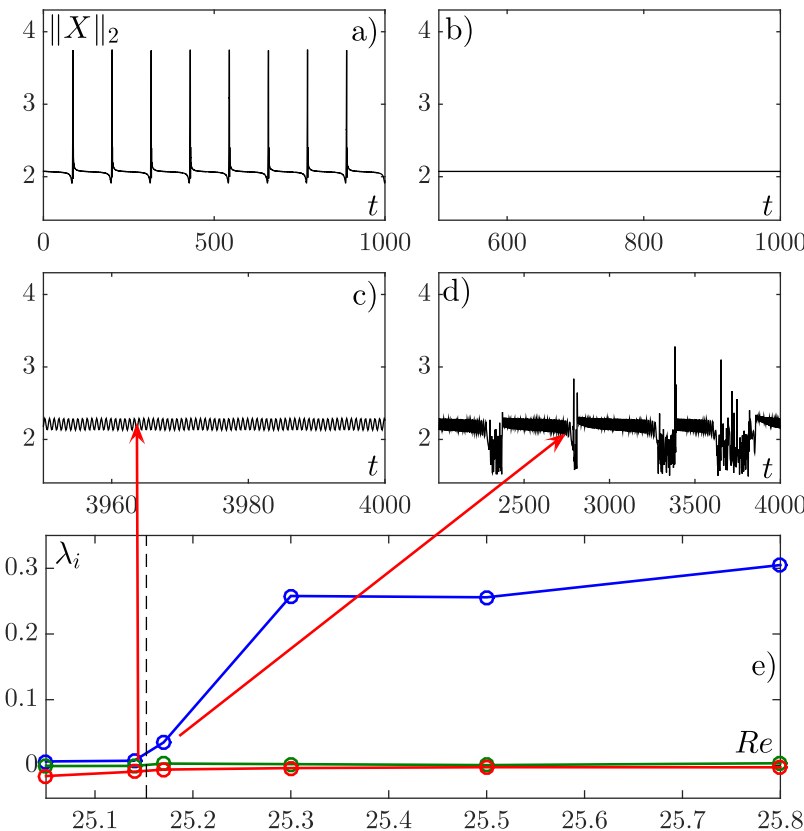


FIG. 23. Time evolution of $\|X\|_2$ is shown for solutions on the drifting branch. Solutions refer to (a) $Re = 21.187$, (b) $Re = 21.194$, (c) $Re = 25.14$, (d) $Re = 25.18$. In (b), there is the drifting solution and in (a) its bursting precursor. In (c), there is the oscillating drift solution and in (d) the intermittent bursting solution. In panel (e) we report the Lyapunov exponents $\lambda_1 > \lambda_2 > \lambda_3$ (marked, respectively, with blue, red, and green empty circles) as functions of Re .

of noise with the main frequencies of the stable solution still present. In the final case (d), the noise becomes predominant and most of the characteristic frequencies have been suppressed.

In Fig. 19, especially in panel (d), we see that the chaotic solutions coming from the period-doubled state disappear until a period-tripled state becomes stable in S5. This branch is shown in panel (e) of Fig. 19 and is characterized by three subsequent period-doubling bifurcations in S6', S6'', and S6'''. The last stable solution is a period 24th-tupling and is shown in the inset of Fig. 22 as a green line. In S6, this state loses its stability and becomes chaotic, as is proved by the Lyapunov exponents in the same figure.

Now we consider the branch of the horizontal drifting solutions. The density stratification is finally strong enough

to affect the bifurcation points of this branch; in particular, a new state before the bifurcation point D3 becomes accessible. The bifurcation of the four traveling solutions (that from D3 lead to the intermittent bursting states) are shifted by the increase in the stratification as we can see from Table I. The difference lies in the appearance, before D3, of a stable branch of bursting solutions, whose L^2 -norm for $Re = 21.187$ is shown in panel (a) of Fig. 23, while in Fig. 24 one can see the contour plots of the vorticity and the temperature [see contour evolution in Fig. 25 (Multimedia view)]. In Fig. 24, are reported the phase portraits of the real and imaginary parts of $\hat{\psi}_k$ and $\hat{\theta}_k$ for $k = (1, 0), (0, 1)$ [respectively, in panels (d) and (g)] and, in panels (i) and (j), at the bursting time, a spike in the time evolution of the Fourier modes is visible. This behavior is described in Ref. 52 in terms of symmetry breaking of

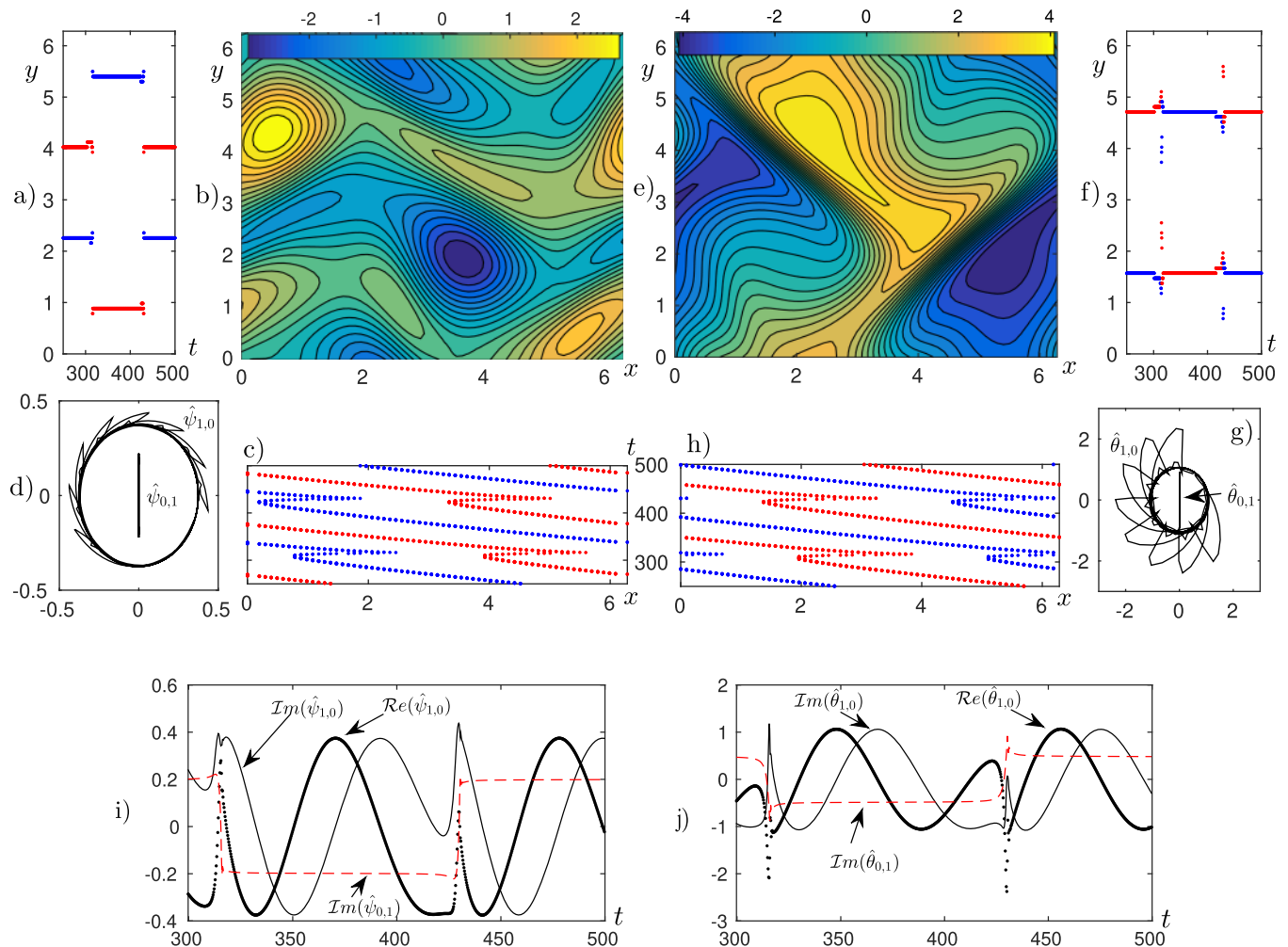


FIG. 24. Stable bursting states when $Re = 21.187$, $Ri = 0.005$, and $Pr = 1$. Contour plots are (b) vorticity and (e) temperature. The temporal position of the extrema of the means is reported in (a) and (c) for vorticity and (f) and (h) for temperature. Red dots stand for maxima, and blue dots stand for minima. The phase portrait of the real and imaginary parts of $\hat{\psi}_k$ and $\hat{\theta}_k$ for $k = (1, 0), (0, 1)$ is shown, respectively, in (d) and (g). Panels (i) and (j) show the trajectories of the real and imaginary parts of mode $(1, 0)$ and the imaginary part of mode $(0, 1)$ for the stream function and temperature in a bursting state.

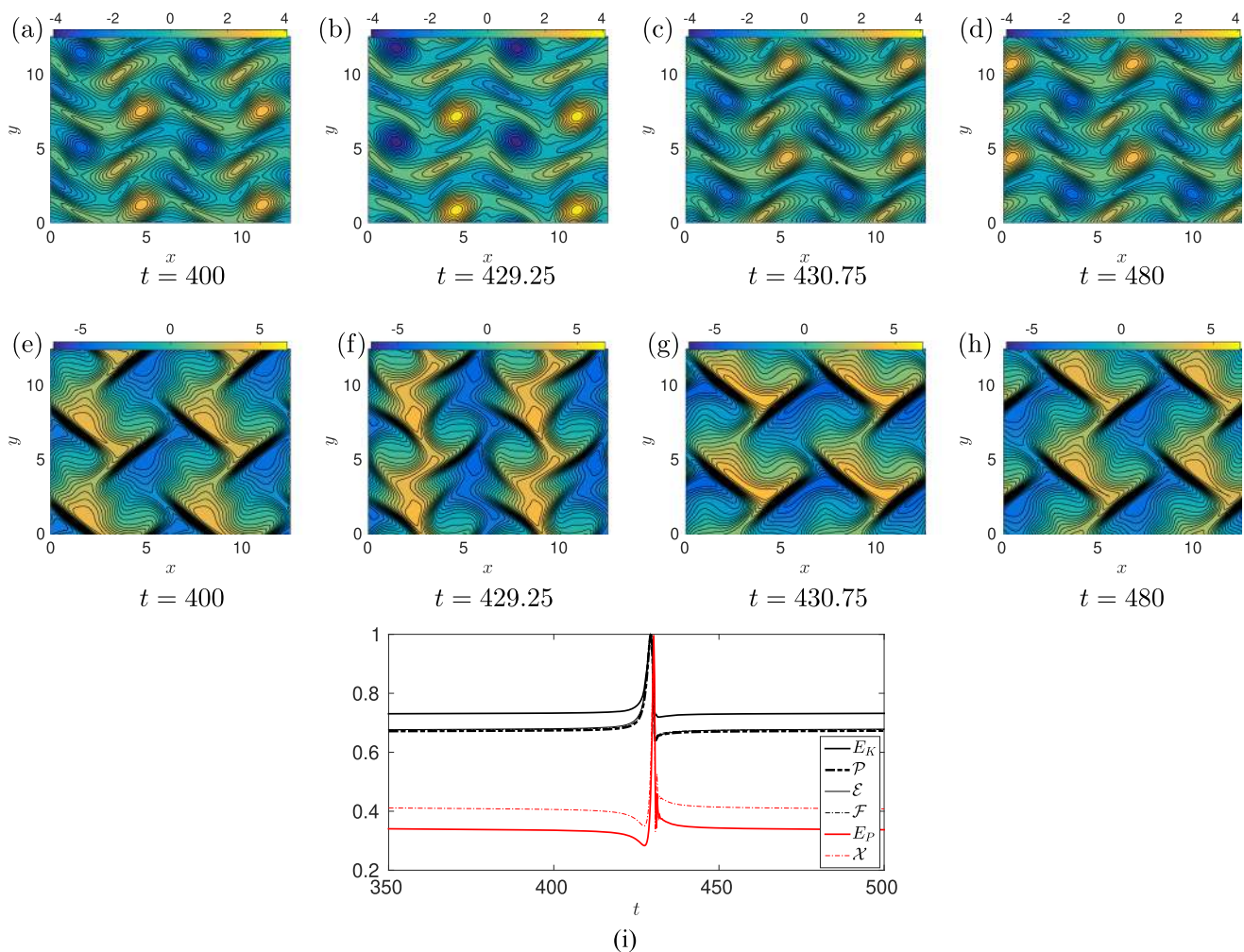


FIG. 25. [(a)–(d)] The vorticity ω and [(e)–(h)] the temperature variation θ , for the stable bursting states when $Re = 21.187$ and $Ri = 0.005$ at various times. (i) Time evolution of kinetic energy E_K , enstrophy \mathcal{E} , palinstrophy \mathcal{P} , kinetic energy growth rate \mathcal{F} , potential energy E_P , and exchange rate \mathcal{X} (all quantities are rescaled with their maximum: $\max E_K = 0.3403$, $\max \mathcal{E} = 1.5809$, $\max \mathcal{P} = 6.8061$, $\max \mathcal{F} = 1.6986$, $\max E_P = 0.0389$, $\max \mathcal{X} = 0.1891$). Multimedia views: <https://doi.org/10.1063/1.5081105.4>; <https://doi.org/10.1063/1.5081105.5>

heteroclinic excursion between spatially organized states, which in this case are drifting states. This branch, which we have been unable to detect for lower Ri , is made of solutions that periodically jump between the four drifting states. In Fig. 25 (Multimedia view), this jump can be observed in the time range $429 \lesssim t \lesssim 430$, when the vorticity field undergoes major rearrangement of the main cores. Notice also how, after a slow build up of the kinetic energy, the jump is characterized by a sudden transfer to potential energy that is then immediately dissipated.

For higher Re , the switching between these states is prevented; see panel (b) of Fig. 23, and in D4, a transition to periodic orbits occurs, as we can see in panel (c) of Fig. 23. The subsequent bifurcation to the bursting solution, also present in less stratified fluid, is proved to be chaotic by the Lyapunov

exponent analysis. In panel (e) of Fig. 23, we show the three larger Lyapunov exponents where one of them becomes positive after D5 (marked as a dashed vertical line).

V. CONCLUSIONS

From the linear stability Richardson number criterion, it is well known that above a threshold—for our system, it is $Ri = 4$ —the laminar state is globally stable. In the region $Ri < 4$, the influence of temperature gradients on the transitions leading to chaotic attractors has not been extensively investigated yet. In this wide range of Richardson number values, we have analyzed the non-stratified fluid and the dynamics of the system in the presence of a weak stratification ($Ri \leq 5 \times 10^{-3}$). We have obtained a refined understanding of

the route to chaos when $Ri = 0$, and we have studied the differences introduced by the stabilizing temperature gradient on the route to chaotic regimes.

The Kolmogorov flow can be considered a theoretical laboratory where, in the last decades, researchers have attempted to get some understanding of the mechanisms of transition phenomena and of fully developed turbulence. One of the underlying ideas is that the attempt to rationalize chaos might give some insight into developed turbulence,²⁸ and in this sense, periodic or recurrent solutions might play a pivotal role. In this paper, we have seen that, in one of the simplest possible settings one can encounter (square domain $[0, 2\pi]^2$, Kolmogorov forcing with $n = 2$, and no stratification $Ri = 0$), a period tripling bifurcation (previously unnoticed) plays a crucial role in an abrupt transition to chaos. The introduction of stratification makes this transition more regular: the period tripling is followed by a sequence of period doubling bifurcations leading, through a typical Feigenbaum scenario, to chaotic solutions. The chaotic states arising from this route are represented by irregular weakening and strengthening of dipolar structures, a feature which is clearly visible in

the irregular behavior of the energy and vorticity dissipations of the flow (respectively, enstrophy and palinstrophy).

New interesting differences are present for $Ri = 0.005$, which is the highest stratification we have considered. In fact, the gluing process of the four Hopf solutions is suppressed while, immediately after the appearance of the glued state, a chaotic window is observed.

We have also observed an overall tendency of the temperature gradient to make horizontal drifting solutions less stable, in the sense that the region of their existence is, in Re terms, smaller. Moreover, in the drifting branch, we have found a new bursting solution, which appears before the horizontally drifting state regains its stability in D3. In general, all the extreme events encountered in our analysis, e.g., the bursting solutions or the abrupt transitions between symmetric configurations, are characterized, in terms of energy balance, first by an accumulation of kinetic energy in the form of strengthening of the vortex cores and then by strong dissipation of this kinetic energy either directly (through viscosity) or through transformation in thermal energy and subsequent dissipation via heat diffusion.

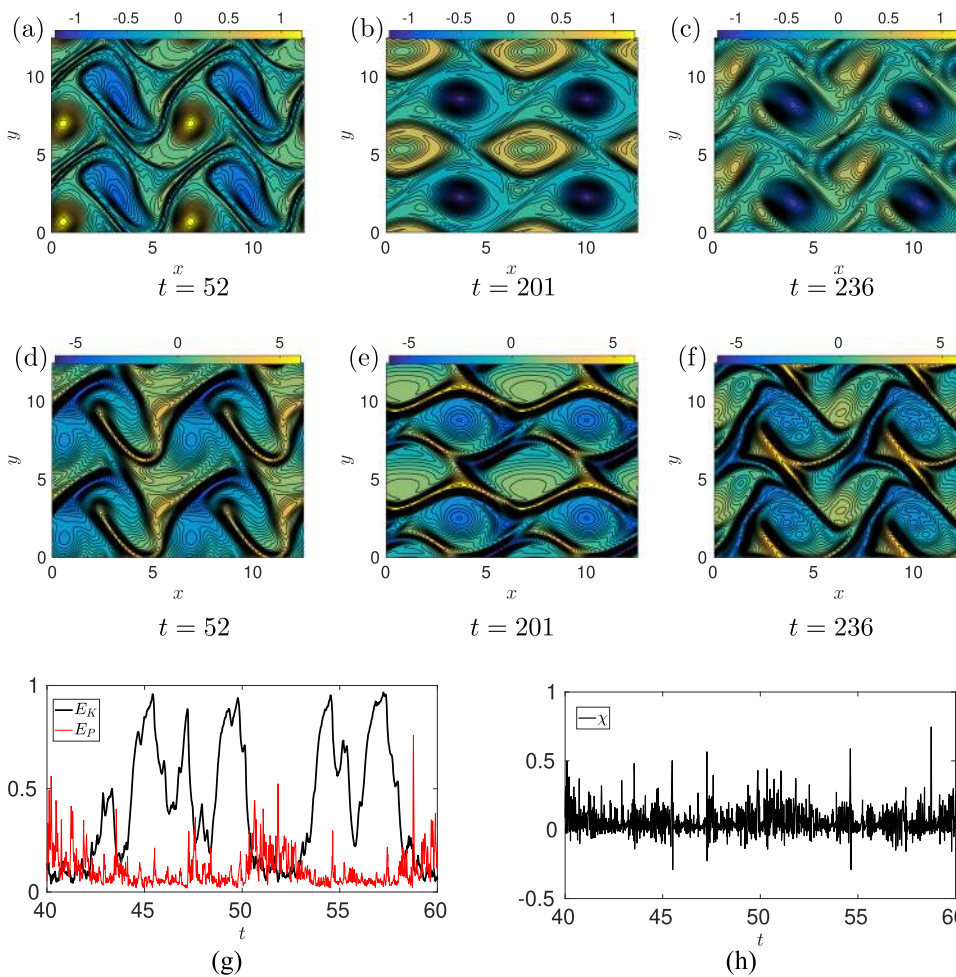


FIG. 26. [(a)–(c)] The vorticity ω and [(d)–(f)] the temperature variation θ for the chaotic state when $Re = 800$, $Ri = 0.001$, $Pr = 1$. (g) Time evolution of kinetic energy E_K and potential energy E_P (all quantities are rescaled with their maximum: $\max E_K = 0.2366$ and $\max E_P = 0.0254$). (h) Time evolution of the energy exchange rate χ (not scaled).

Several problems have been neglected by our analysis and suggest themselves as possible topics of future investigations; here we mention few of them. In this paper, we have chosen to restrict ourselves to weak stratification so that the main focus has been to understand how the presence of stratification modifies the solutions one encounter in the classical $Ri = 0$ case. Some surveying simulations with $Ri > 0.005$ have revealed completely new states, and there is plenty to explore in the region $0.005 < Ri < 4$, which is also interesting from the physical point of view, e.g., because geophysical flows mostly belong to this class. One would expect that by increasing the Ri , potential energy and kinetic energy become the same order of magnitude, the fact that the energy introduced by the external forcing can be more easily buffered (and, after a threshold is passed, then suddenly released) and can make more likely bursting solutions or subcritical transitions. How this would modify the route to chaos is completely open and will be the subject of future work.

Other restrictions that we have adopted are to consider a domain with an aspect ratio $\alpha = 1$ and the Kolmogorov forcing with $n = 2$; clearly a more complex setting would lead to flows with an even richer structure, and also this we believe is worth being investigated; just as an example, it would be interesting to see how stratification modifies the behavior of the localized chaotic structures that one encounter in flows over large domains.²⁵

Finally, a challenging topic would be to see how and whether the chaotic structures we have described in this paper evolve into fully developed turbulent structures with increasing Reynolds numbers. Some simulations performed up to $Re = O(10^3)$ seem to suggest that the flow recurrently visits some of the coherent structures we have encountered in the present paper, and it would be interesting to confirm (or disprove) this and see if this could be of some use in the description of turbulent flows.^{13,28,39,53,54} In Fig. 26, we show three snapshots of the flow at $Re = 800$, $Ri = 0.001$, $Pr = 1$. For this high Re , small-scale vortical structures appear with sharper variations in the vorticity field; however, these structures recurrently coalesce to more coherent patterns, some of them being already observed in the low Re regime: in panels (a) and (c) of Fig. 26, we can recognize vortical structures similar to the steady state reported in Fig. 3(a). In panels (b) and (e), a typical cat's eye pattern is visible in vorticity and temperature variation. The overall evolution is globally chaotic with rapid variation in kinetic and potential energy [see panel (g)]. This high Re regime is characterized by an energy balance which is totally in contrast to that observed for the low Re regime analyzed throughout the paper: in fact the conversion from potential to kinetic energy is now clearly present, as shown in panel (h). We also mention that it would be interesting to see whether, for the stratified case, the unimodal solutions⁵⁵ encountered in the classical Kolmogorov flow persist.

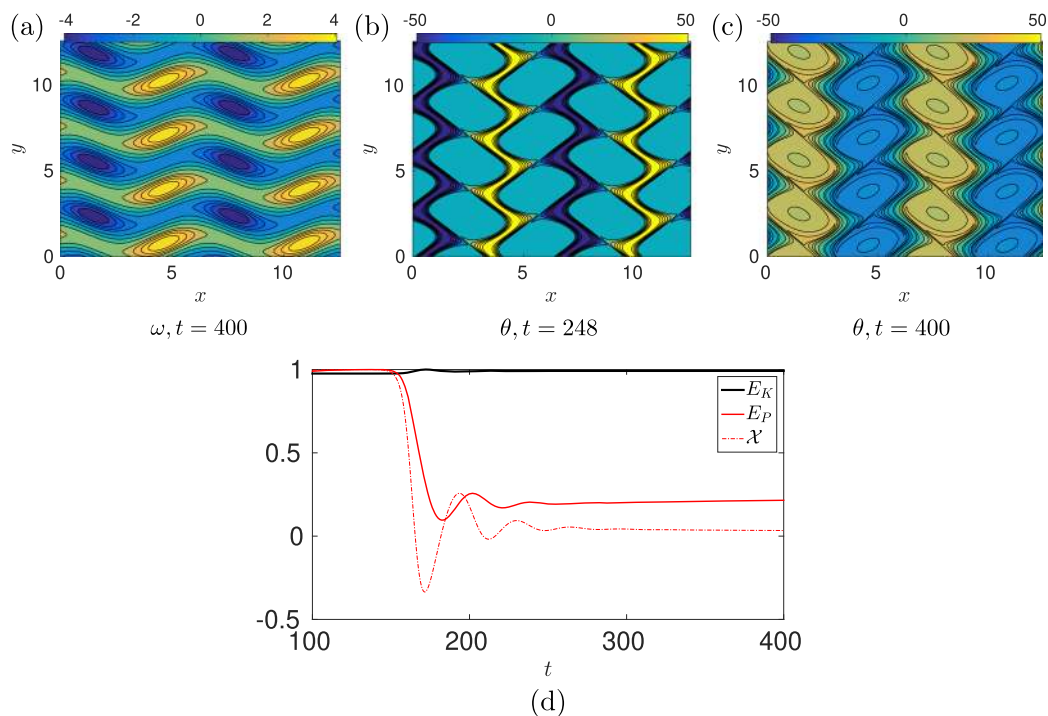


FIG. 27. (a) The vorticity ω and [(b) and (c)] the temperature variation θ , for the drifting state when $Re = 4$, $Ri = 0.001$, and $Pr = 500$ at various time. (d) Time evolution of kinetic energy E_K , potential energy E_P , and exchange rate \mathcal{X} (all quantities are rescaled with their maximum: $\max E_K = 0.7221$, $\max E_P = 1.0270$, $\max \mathcal{X} = 0.0275$).

When $Re \gg 1$, the vorticity equation becomes singularly perturbed and vorticity layers are expected to appear. If moreover $Pr = O(1)$, the system is in the large Péclet number ($Pe = Re \cdot Pr$) regime and, being also the equation for the temperature singularly perturbed,³¹ thermal internal layers will develop; in Fig. 26, one can in fact observe sharp transition regions, both in temperature and vorticity field. For large Pr and $Re = O(1)$, a different behavior is however observed: sharp transitions appear in temperature field only, whereas smoother behavior is seen in the vorticity field. In Fig. 27, the case $Pr = 500$, $Re = 4$, $Ri = 0.001$ is shown; the flow sets to a horizontally drifting state where the vorticity has the same structure of the state shown in Fig. 10(a), whereas a checkboard-like pattern appears in the temperature variation [panel (d)] with very strong gradients. These behaviors are very similar to those reported in Ref. 31, where the same Pe regime was analyzed. For large Pr , we expect a highly complex transition scenario, whose analysis is left to future work.

ACKNOWLEDGMENTS

The authors thank the referees for valuable suggestions and comments that helped improving the presentation of the paper. This work has been partially supported by INdAM-GNFM.

APPENDIX: RICHARDSON LINEAR STABILITY CRITERION

For completeness in this section, we mention how to study the linear instability of a horizontal wave perturbation $[\psi, \theta] = [\hat{\psi}, \hat{\theta}] \exp[ik(x - ct)]$ induced on the laminar state $\Psi_0 = \sin ny$ and $\theta_0 = y$. More details can be found in Refs. 31 and 56. The main purpose is to provide the Richardson number stability criterion under our non-dimensional parameter setups. The eigenvalue problem is

$$\left(\frac{d^2}{dy^2} - k^2\right)^2 \hat{\psi} - ik(nRe \cos ny - c) \left(\frac{d^2}{dy^2} - k^2\right) \hat{\psi} - n^3 ik Re \hat{\psi} \cos ny - ik Re Ri \hat{\theta} = 0, \tag{A1}$$

$$\frac{1}{Pr} \left(\frac{d^2}{dy^2} - k^2\right) \hat{\theta} - ik(nRe \cos ny - c) \hat{\theta} + ik Re \hat{\psi} = 0. \tag{A2}$$

We look for the marginal stability curve when $c = 0$. In the inviscid limit, we find the Taylor–Goldstein equations

$$\frac{d^2 \hat{\psi}}{dy^2} + \left(n^2 - k^2 + \frac{Ri}{n^2 \cos^2 ny}\right) \hat{\psi} = 0. \tag{A3}$$

To solve this differential equation, we write (A3) as the product of two operators,

$$\mathcal{L} \mathcal{L}^\dagger = \left[\frac{d^2}{dy^2} + n^2 - k^2 + \frac{Ri}{n^2 \cos^2 ny}\right], \tag{A4}$$

where the linear differential operators are $\mathcal{L} \equiv \frac{d}{dy} + a \tan ny$ and $\mathcal{L}^\dagger \equiv \frac{d}{dy} - a \tan ny$. The parameters a and Ri depend on k

according to

$$a^2 = n^2 - k^2, \quad Ri = n^3 \sqrt{n^2 - k^2} - n^2 (n^2 - k^2). \tag{A5}$$

From the last equation, we can easily observe that the Richardson number has a maximum when $k_c = n\sqrt{3}/2$ and $Ri(k_c) = n^4/4$; thus, the Richardson number stability criterion is $Ri < 4$ for our model setup $n = 2$.

REFERENCES

- ¹V. Arnol'd and L. Meshalkin, "Seminar led by A. N. Kolmogorov on selected problems of analysis (1958-1959)," *Usp. Mat. Nauk* **15**, 20-24 (1960).
- ²L. Meshalkin and I. G. Sinai, "Investigation of the stability of a stationary solution of a system of equations for the plane movement of an incompressible viscous liquid," *J. Appl. Math. Mech.* **25**, 1700-1705 (1961).
- ³C. Marchioro, "An example of absence of turbulence for any Reynolds number," *Commun. Math. Phys.* **105**, 99-106 (1986).
- ⁴G. Sivashinsky, "Weak turbulence in periodic flows," *Physica D* **17**, 243-255 (1985).
- ⁵A. Nepomniashchii, "On stability of secondary flows of a viscous fluid in unbounded space: PMM vol. 40, no. 5, 1976, pp. 886-891," *J. Appl. Math. Mech.* **40**, 836-841 (1976).
- ⁶D. Armbruster, B. Nicolaenko, N. Smaoui, and P. Chossat, "Symmetries and dynamics for 2-D Navier-Stokes flow," *Physica D* **95**, 81-93 (1996).
- ⁷Z.-S. She, "Metastability and vortex pairing in the Kolmogorov flow," *Phys. Lett. A* **124**, 161-164 (1987).
- ⁸B. Nicolaenko and Z.-S. She, "Coherent structures, homoclinic cycles and vorticity explosions in Navier-Stokes flows," in *Topological Fluid Mechanics* (Cambridge, 1989) (Cambridge University Press, Cambridge, 1990), pp. 265-277.
- ⁹N. Platt, L. Sirovich, and N. Fitzmaurice, "An investigation of chaotic Kolmogorov flows," *Phys. Fluids A* **3**, 681-696 (1991).
- ¹⁰V. Franceschini, C. Tebaldi, and F. Zironi, "Fixed point limit behavior of N-mode truncated Navier-Stokes equations as N increases," *J. Stat. Phys.* **35**, 387-397 (1984).
- ¹¹M. Kurganskii, "Instability of internal gravity waves propagating at small angles to the vertical," *Izv. Akad. Nauk SSSR, Fiz. Atmos. Okeana* **16**, 1024-1033 (1980).
- ¹²G. Gambino, M. Lombardo, and M. Sammartino, "Adaptive control of a seven mode truncation of the Kolmogorov flow with drag," *Chaos, Solitons Fractals* **41**, 47-59 (2009).
- ¹³D. Lucas and R. Kerswell, "Recurrent flow analysis in spatiotemporally chaotic 2-dimensional Kolmogorov flow," *Phys. Fluids* **27**, 045106 (2015).
- ¹⁴E. Lorenz, "Barotropic instability of Rossby wave motion," *J. Atmos. Sci.* **29**, 258-264 (1972).
- ¹⁵E. Sasaki, S. I. Takehiro, and M. Yamada, "Bifurcation structure of two-dimensional viscous zonal flows on a rotating sphere," *J. Fluid Mech.* **774**, 224-244 (2015).
- ¹⁶A. Manfroi and W. Young, "Slow evolution of zonal jets on the beta plane," *J. Atmos. Sci.* **56**, 784-800 (1999).
- ¹⁷N. Bondarenko, M. Gak, and F. Dolzhanskiy, "Laboratory and theoretical models of plane periodic flows," *Izv., Atmos. Oceanic Phys.* **15**, 711-716 (1979).
- ¹⁸B. Suri, J. Tithof, R. Mitchell, Jr., R. Grigoriev, and M. Schatz, "Velocity profile in a two-layer Kolmogorov-like flow," *Phys. Fluids* **26**, 053601 (2014).
- ¹⁹J. M. Burgess, C. Bizon, W. D. McCormick, J. B. Swift, and H. L. Swinney, "Instability of the Kolmogorov flow in a soap film," *Phys. Rev. E* **60**, 715-721 (1999).
- ²⁰A. M. Batchaev, "Laboratory simulation of the Kolmogorov flow on a spherical surface," *Izv., Atmos. Oceanic Phys.* **48**, 657-662 (2012).
- ²¹A. Batchaev and M. Kurgansky, "Periodic shear flow instability in a weakly stratified fluid," *Izv., Atmos. Oceanic Phys.* **22**, 1-5 (1986).

- ²²A. Batchaev, V. Dovzhenko, and M. Kurgansky, "Simulation of shear flow in a stratified fluid," *Izv., Atmos. Oceanic Phys.* **20**, 439–442 (1984).
- ²³G. Ponetti, M. Sammartino, and V. Sciacca, "Formation of coherent structures in Kolmogorov flow with stratification and drag," *Acta Appl. Math.* **132**, 483–492 (2014).
- ²⁴P. Caillol, "Nonlinear internal waves in the upper atmosphere," *Geophys. Astrophys. Fluid Dyn.* **99**, 271–308 (2005).
- ²⁵D. Lucas and R. Kerswell, "Spatiotemporal dynamics in two-dimensional Kolmogorov flow over large domains," *J. Fluid Mech.* **750**, 518–554 (2014).
- ²⁶A. Thess, "Instabilities in two-dimensional spatially periodic flows. Part I: Kolmogorov flow," *Phys. Fluids A* **4**, 1385–1395 (1992).
- ²⁷H. Okamoto and M. Shoji, "Bifurcation diagrams in Kolmogorov's problem of viscous incompressible fluid on 2-D flat tori," *Jpn. J. Ind. Appl. Math.* **10**, 191–218 (1993).
- ²⁸G. Chandler and R. Kerswell, "Invariant recurrent solutions embedded in a turbulent two-dimensional Kolmogorov flow," *J. Fluid Mech.* **722**, 554–595 (2013).
- ²⁹P. Davis and W. Peltier, "Resonant parallel shear instability in the stably stratified planetary boundary layer," *J. Atmos. Sci.* **33**, 1287–1300 (1976).
- ³⁰P. Garaud, B. Gallet, and T. Bischoff, "The stability of stratified spatially periodic shear flows at low Péclet number," *Phys. Fluids* **27**, 084104 (2015).
- ³¹N. Balmforth and Y. Young, "Stratified Kolmogorov flow," *J. Fluid Mech.* **450**, 131–167 (2002).
- ³²G. Ponetti, M. Sammartino, and V. Sciacca, "Transitions in a stratified Kolmogorov flow," *Ric. Mat.* **66**, 189–199 (2017).
- ³³H. Lamela, G. Carpintero, and F. Mancebo, "Period tripling and chaos in the dynamic behavior of directly modulated diode lasers," *IEEE J. Quantum Electron.* **34**, 1797–1801 (1998).
- ³⁴B. Goswami, "Observation of some new phenomena involving period tripling and period doubling," *Int. J. Bifurcation Chaos* **05**, 303–312 (1995).
- ³⁵B. Goswami, "Self-similarity in the bifurcation structure involving period tripling, and a suggested generalization to period n-tupling," *Phys. Lett. A* **245**, 97–109 (1998).
- ³⁶A. Libchaber and J. Maurer, "A Rayleigh Bénard experiment: Helium in a small box," in *Nonlinear Phenomena at Phase Transitions and Instabilities*, NATO Advanced Study Institutes Series Vol. 77, edited by T. Riste (Springer US, 1982), pp. 259–286.
- ³⁷C. Hamakiotes and S. Berger, "Periodic flows through curved tubes. The effect of the frequency parameter," *J. Fluid Mech.* **210**, 353–370 (1990).
- ³⁸O. Bendiksen, "Nonlinear mode interactions and period-tripling flutter in transonic flow," *J. Fluids Struct.* **19**, 591–606 (2004).
- ³⁹M. Barjona and C. B. da Silva, "Kolmogorov's Lagrangian similarity law revisited," *Phys. Fluids* **29**, 105106 (2017).
- ⁴⁰A. Wolf, J. B. Swift, H. L. Swinney, and J. A. Vastano, "Determining Lyapunov exponents from a time series," *Physica D* **16**, 285–317 (1985).
- ⁴¹H. Clercx and C.-H. Bruneau, "The normal and oblique collision of a dipole with a no-slip boundary," *Comput. Fluids* **35**, 245–279 (2006).
- ⁴²W. Kramer, H. Clercx, and G. van Heijst, "Vorticity dynamics of a dipole colliding with a no-slip wall," *Phys. Fluids* **19**, 126603 (2007).
- ⁴³F. Gargano, M. Sammartino, and V. Sciacca, "High Reynolds number Navier-Stokes solutions and boundary layer separation induced by a recirculating vortex," *Comput. Fluids* **52**, 73–91 (2011).
- ⁴⁴F. Gargano, M. Sammartino, V. Sciacca, and K. Cassel, "Analysis of complex singularities in high-Reynolds-number Navier-Stokes solutions," *J. Fluid Mech.* **747**, 381–421 (2014).
- ⁴⁵R. Caflisch, F. Gargano, M. Sammartino, and V. Sciacca, "Complex singularities and PDEs," *Riv. Mat. Univ. Parma* **6**, 69–133 (2015).
- ⁴⁶H. Clercx and G. van Heijst, "Dissipation of coherent structures in confined two-dimensional turbulence," *Phys. Fluids* **29**, 111103 (2017).
- ⁴⁷D. Ayala and B. Protas, "Maximum palinstrophy growth in 2D incompressible flows," *J. Fluid Mech.* **742**, 340–367 (2014).
- ⁴⁸Y. Kimura and J. Herring, "Gradient enhancement and filament ejection for a non-uniform elliptic vortex in two-dimensional turbulence," *J. Fluid Mech.* **439**, 43–56 (2001).
- ⁴⁹B. Brummer and M. Schultze, "Analysis of a 7-year low-level temperature inversion data set measured at the 280m high Hamburg weather mast," *Meteorol. Z.* **24**, 481–494 (2015).
- ⁵⁰M. Inubushi, M. U. Kobayashi, S. Takehiro, and M. Yamada, "Covariant Lyapunov analysis of chaotic Kolmogorov flows and time-correlation function," *Procedia IUTAM* **5**, 244–248 (2012).
- ⁵¹C. Godrèche and P. Manneville, *Hydrodynamics and Nonlinear Instabilities*, Collection Alea-Saclay: Monographs and Texts in Statistical Physics (Cambridge University Press, 1998).
- ⁵²B. Nicolaenko and Z.-S. She, "Turbulent bursts, inertial sets and symmetry-breaking homoclinic cycles in periodic Navier-Stokes flows," in *Turbulence in Fluid Flows*, IMA Volumes in Mathematics and its Applications Vol. 55 (Springer, New York, 1993), pp. 123–136.
- ⁵³P. Cvitanović and J. Gibson, "Geometry of the turbulence in wall-bounded shear flows: Periodic orbits," *Phys. Scr., T* **142**, 014007 (2010).
- ⁵⁴G. C. Layek and Sunita, "Non-Kolmogorov scaling and dissipation laws in planar turbulent plume," *Phys. Fluids* **30**, 115105 (2018).
- ⁵⁵S.-C. Kim and H. Okamoto, "Unimodal patterns appearing in the Kolmogorov flows at large Reynolds numbers," *Nonlinearity* **28**, 3219–3242 (2015).
- ⁵⁶P. G. Drazin and W. H. Reid, *Hydrodynamic Stability* (Cambridge University Press, 2004).